This is the peer-reviewed, final accepted version for American Mineralogist, published by the Mineralogical Society of America.
The published version is subject to change. Cite as Authors (Year) Title. American Mineralogist, in press.
DOI: https://doi.org/10.2138/am-2023-9217. http://www.minsocam.org/

Revision 1

Enrichment and fractionation of rare earth elements (REEs) in ion-adsorption-type REE deposits: Constraints of an iron (hydr)oxide–clay mineral composite

XIAOLIANG LIANG [1, 3, *], PUQIU WU [1, 3], GAOLING WEI [2], YIPING YANG [1], SHICHAO JI [1], LINGYA MA [1, 3], JINGWEN ZHOU [1, 3], WEI TAN [1, 3], JIANXI ZHU [1, 3], YOSHIO TAKAHASHI [4]

[1] CAS Key Laboratory of Mineralogy and Metallogeny/Guangdong Provincial Key Laboratory of Mineral Physics and Materials, Guangzhou Institute of Geochemistry, Chinese Academy of Sciences, Guangzhou 510640, P.R. China;

[2] National-Regional Joint Engineering Research Center for Soil Pollution Control and Remediation in South China, Guangdong Key Laboratory of Integrated Agro-environmental Pollution Control and Management, Institute of Eco-environmental and Soil Sciences, Guangdong Academy of Sciences, Guangzhou, 510650, P.R. China;

[3] University of Chinese Academy of Sciences, Beijing 100049, P.R. China;

[4] Department of Earth and Planetary Science, Graduate School of Science, The University of Tokyo, 7-3-1, Hongo, Bunkyo-ku, Tokyo 113-0033, Japan.

[*] Corresponding author. E-mail: liangxl@gig.ac.cn (X.L. LIANG). [#] The authors contribute equally.

ABSTRACT

Ion-adsorption-type rare earth element (REE) deposits are the source of more than 90% of global heavy REEs (HREEs). Thus, understanding the ore genesis of REEs, particularly the distribution characteristics and enrichment mechanisms of HREEs, is vital for efficient exploration and mining of ion-adsorption-type REE deposits worldwide. The characteristics and petrogenesis of bedrock, and the aqueous mobility of REEs, are known to be important factors controlling REE accumulation and fractionation in the weathering crust of REE deposits. However, the effect of REE adsorption on secondary minerals, which is a crucial step in deposit formation, remains poorly understood. This problem was addressed by the study described herein, which involved a systematic analysis of the complete weathering profile (78 m) of the Renju ion-adsorption-type REE deposit in South China and a simulated adsorption experiment. Clay minerals and iron (Fe) (hydr)oxides are the dominant REE adsorbents in the weathering crust and most are micro-to-nanosized particles. Thus, the fine particle fraction (< 2 μm) was separated from field samples, to better disclose their effects on the concentration and redistribution of REEs. Phase compositions and morphologies were characterized by X-ray diffraction, Mössbauer spectrometry, and scanning/transmission electron microscopy (SEM/TEM), which revealed that various clay minerals and Fe (hydr)oxides form composites along the profile of the deposit. Composites of ferrihydrite–kaolinite, goethite–kaolinite/halloysite, and hematite–kaolinite/halloysite were found to be distributed in the semi-weathered, completely weathered, and topsoil layers, respectively, with different sizes and shapes. The

concentrations and partition patterns of REEs in different occurrence states were distinguished after sequential extraction. Ion-exchangeable-REEs were the major state and enriched in the upper completely weathered layer. These species were found to be adsorbed onto kaolinite and halloysite via electrostatic attraction, without obvious fractionation. Fe (hydr)oxides were determined to comprise ca. 20% of REEs at most depths and over 50% of REEs in the topsoil and semi-weathered layer. It was found that Fe (hydr)oxides scavenge REEs through complexation and oxidation, resulting in HREE enrichment and a positive cerium (Ce) anomaly, respectively. In addition, compared with crystalline Fe (hydr)oxides, amorphous Fe (hydr)oxides immobilize more REEs but exhibit weaker preferential adsorption of HREEs. The above-described findings are consistent with the results of simulated experiments for REE adsorption onto a clay mineral–Fe (hydr)oxide composite (Bt-60), which was obtained from hydrothermal processing of biotite. Furthermore, the distributions and stabilities of LREEs and HREEs were distinguished by TEM–energy–dispersive spectroscopy (EDS) of Bt-60 before and after REE extraction by ammonium sulfate. The phase transformation pathways of clay minerals and Fe (hydr)oxides, and their different enrichment and fractionation characteristics in REEs, were also discussed in terms of the structure and surface properties of minerals, adsorption mechanisms, and variations in chemical properties across the REE group. The results shed new light on how clay minerals and Fe (hydr)oxides affect the enrichment and fractionation of REEs in ion-adsorption-type deposits.

Keywords: Ion-adsorption-type REE deposit; clay minerals; Fe (hydr)oxides;

adsorption; fractionation; weathering

INTRODUCTION

Rare earth elements (REEs) encompass lanthanide-group elements plus yttrium (Y) and scandium, and are critical metals for various modern industries. Compared to light REEs (LREEs; lanthanum (La) to europium (Eu)), there are lower crustal concentrations of heavy REEs (HREEs; gadolinium (Gd) to lutetium (Lu) + yttrium (Y)), but HREEs are more important in renewable energy and high-technology industries (Chakhmouradian and Wall, 2012). The growing demand for HREEs coupled with the decrease in HREE supplies from China has led to HREE resources to become a popular exploration target worldwide. Currently, ion-adsorption-type REE deposits account for more than 90% of global HREE supply (Borst et al., 2020), and thus have become a focus of interest.

To date, over 200 ion-adsorption-type REE deposits have been identified predominantly in South China (Sanematsu and Watanabe, 2016), with sporadic identification globally, e.g., Madagascar (Berger et al., 2014), the Democratic Republic of Congo (Kasay et al., 2022), Brazil (Costa et al., 2020), and Southeast Asia (Sanematsu et al., 2013). These deposits are generated by *in-situ* weathering processes and thus are invariably located in temperate or tropical regions, where the moderate-to-high temperatures, precipitation rates and strong microbial activities facilitate the decomposition of REE-bearing minerals and the downward transfer of soluble REEs (Li et al., 2022). Subsequently, aqueous REEs are adsorbed onto secondary minerals

and accumulated in regolith, resulting in the fractionation into LREEs and HREEs (Li et al., 2019). Interestingly, only 10% of REE deposits are enriched in HREEs, with the total concentration (∑) of HREE oxides comprising greater than 50% of the total REE resource (Li et al., 2019). Nevertheless, in all of these deposits, compared with the concentrations of REEs (and especially HREEs) in parent rocks, those in regolith can be up to ten-fold greater. Thus, it is imperative to systematically investigate the enrichment of HREEs during the weathering of REE deposits to enhance the understanding of ore formation.

Various factors have been reported to control the redistribution and fractionation of REEs, such as the composition of REE-bearing minerals in parent rocks (Xu et al., 2017), solution complexation and differential mobilities of REE complexes (Quinn et al., 2006), and adsorption of REEs by secondary minerals (Coppin et al., 2002). It is generally accepted that the REE patterns in regolith are largely inherited from those in parent rocks and that HREE-enriched deposits predominantly develop on highly differentiated muscovite granites (Li et al., 2017). In parent rock, fragile HREE-bearing minerals including parasite-(Y), synchysite-(Y), titanite, and gadolinite, are the source of HREEs (Li et al., 2017). During the weathering process, REE-bearing minerals are decomposed by acidic soil water at shallow depths, leading to the release of REE ions into leachate. REE ions then form complexes with organic or inorganic substances, or transfer as REE(III), and migrate downward (Li et al., 2021; Tang and Johannesson, 2010). Compared with LREEs, HREEs bind more strongly to several ligands (e.g., humic acid, fluoride, and carbonate) (Luo and Byrne, 2004). Thus, LREEs typically

accumulate at shallow depths, whereas HREEs are transported to deeper depths (Li et al., 2019). As pH increases with depth, REEs are adsorbed onto secondary minerals, e.g., clay minerals and Fe (hydr)oxides (Borst et al., 2020). However, compared with what is known regarding parent rock and solution complexation, the effect of adsorption on the fractionation between LREEs and HREEs has been less explicit, especially in terms of the following aspects.

(1) Clay minerals, typically kaolinite and halloysite, are the primary adsorbents of REEs. The adsorption experiment showed that although REE adsorption increased with pH, there was no fractionation under reaction conditions identical to those in soil and ground water (Yang et al., 2019). However, calculations showed that LREEs are preferentially adsorbed by clay minerals (Coppin et al., 2002). Additionally, in the presence of high concentrations of ligands (e.g., humic acid and carbonate), more aqueous LREEs than HREEs were removed by kaolinite, whereas HREEs were strongly complexed and remained in solution. REE adsorption is also affected by the properties of minerals, e.g., crystallinity, morphology, and surface properties. For example, in the Zudong deposit, the world's largest regolith-hosted HREE deposit, weathering transforms microcrystalline kaolinite into large, highly crystalline vermicular kaolinite, with the latter having the specific surface area (SSA), porosity, and adsorption-site availability that are substantially different from those of the former (Li and Zhou, 2020). These variations probably give rise to the contrasting adsorption ability of different soil horizons and accordingly the redistribution of REEs, although this has yet to be confirmed by careful analysis of field samples.

(2) In addition to clay minerals, Fe (hydr)oxides are ubiquitous in regolith and are formed by the dissolution and recrystallization of ferric silicate minerals, e.g., biotite and chlorite in the bedrock (Galán and Ferrell, 2013). With large surface areas, abundant surface hydroxyl groups, and strong oxidation abilities, Fe (hydr)oxides are important REE scavengers (Ohta et al., 2009a). Sequential extraction of a typical weathering crust revealed that the REE concentration in Fe (hydr)oxide-associated fraction was second only to that in an ion-exchangeable fraction (Huang et al., 2021b). Moreover, Fe (hydr)oxides can immobilize REEs through surface complexation and have a higher adsorption capacity for HREEs than LREEs (Ohta et al., 2009b). This implies that REE adsorption on Fe (hydr)oxides is crucial for their fractionation and availability, which has yet to be comprehensively investigated.

(3) During progressive weathering, both Fe (hydr)oxides and clay minerals undergo crystallization and phase transformation (Cornell and Schwertmann, 1996; Galán and Ferrell, 2013). In most cases, Fe (hydr)oxide particles adhere to clay minerals to form nanosized composites. This decreases the particle sizes and thus increases their SSAs, which in turn increases the adsorption capacity for REEs. On the other hand, the loading of Fe (hydr)oxides onto clay minerals causes a shift in the zero point of charge (ZPC) to a higher pH (Sakurai et al., 1990). This suggests that the adsorption capacities of composites for REEs differ from those of individuals. However, little is known about the phase composition, surface properties, and REE adsorption capacities of Fe (hydr)oxide and clay mineral composites in the weathering crust, or their relative contributions to REE enrichment and fractionation.

Accordingly, in this study, the Renju ion-adsorption-type REE deposit was investigated. Weathering profile samples were collected from the deposit by core drilling, and then particles less than 2 μm in size were extracted and used as the object of this study. This approach was used for two reasons. Most clay minerals and Fe (hydr)oxides are smaller than 2 μm in such deposits. On the other hand, secondary REE-bearing minerals, e.g., apatite, allanite, monazite, etc, are absent from fine particle samples, which facilitates sequential extraction-based analysis and nanoscale morphological observation. Additionally, compared with coarse particles, fine particles have larger SSAs and higher mobilities, and thus are more involved in the transport and enrichment of REEs (Li and Zhou, 2020). The obtained fine particle samples were analyzed to determine their mineral compositions and surface properties, and the type and concentrations of REE species they contained. REE-adsorption simulation experiments were also carried out using hydrothermally treated biotite, followed by microscopic characterization.

SAMPLEING AND ANALYTICAL METHODS

Geological background

The Renju deposit is located in Pingyuan County, Meizhou City, Guangdong Province, South China. The deposit contains a total rare-earth oxide (REO) resource of 20,467 tons with a grade of 0.153%-0.197% REOs. It is hosted in the weathered crust of the Renju pluton, an early Yanshanian granitoid pluton with an exposed area of 29.3 km^2. The Renju granites consist of biotite granite, granite porphyry and quartz diorite.

More details on the geological background of Renju deposit are provided in Figure S1 and Text S1.

Sampling and sample preparation

A 78.0-m-long drill core from laterite to fresh granitewas extracted using a custom-made double-tube drilling system. The outermost part of each sample in the drill core was scraped off, and then the uncontaminated samples from different weathering stages were collected by quartering.

The fraction of fine particles (<2 μm) was collected as follows. First, a 250-g sample was added to a 5-L cylinder filled with deionized water, and the resulting suspension was dispersed by vigorous shaking and ultrasonication in a bath for 15 min. Next, the fine particle fraction was obtained through sedimentation for 25 h, according to Stokes' law (Anderson et al., 1981), and subsequently dried at 60 °C to drive off non-crystalline water.

Sample characterization

Particle size distribution

The particle size distributions of samples were analyzed on an LS I3 320 laser-diffraction particle size analyzer, which had a detection range of 0.2–2000 μm and an error of less than 5%.

pH measurement

The pH of samples was measured through the following procedure. A 10-g sample was mixed with 25 mL of deionized water. The resulting suspension was stirred for 8 h, and the pH of the liquid supernatant was monitored using a Mettler-Toledo FiveEasy Plus™ pH meter.

X-ray diffraction (XRD) analysis

XRD patterns were collected from 2° to 70° (2θ) for powder samples and oriented samples at a scanning speed of $3°\cdot min^{-1}$ on a Bruker D8 Advance X-ray diffractometer, operated at 40 kV and 40 mA, using nickel (Ni)-filtered copper (Cu) K-α radiation. Oriented samples were prepared by carefully pipetting a clay suspension onto a glass slide and allowing the coated slide to air-dry at room temperature. Some of the resulting samples were solvated with ethylene glycol vapor in a glass desiccator at 60 °C for 24 h. This allowed ethylene glycol to intercalate into any swelling clay minerals (e.g., montmorillonite and chlorite) that were present, thereby causing their interlayer spacing to increase, which would be demonstrated by the shifting of their (001) diffraction peak to a low angle. Similarly, formamide intercalation was used to detect the presence of kaolinite and halloysite (Churchman et al., 1984). Thus, some of the oriented samples were sprayed with formamide solution and then air dried for 2 h. After such a treatment, halloysite has basal spacing of 10–11 Å, whereas kaolinite retains its original basal spacing, i.e., ca. 7 Å. The relative proportions of these two minerals were determined by computing $I_{10}/(I_7 + I_{10})$ ratios from the XRD patterns, in which I_7 and I_{10} denote the intensity peaks near 7 and 10 Å, respectively. Refinement and quantification of powder

XRD data were conducted using Java Agent Development Framework 6.5 software.

Major element analysis

Samples were dry-ashed at 900 °C to remove carbonate and organic matter. Subsequently, approximately 0.50 g of each treated sample was combined with 4 g of a flux composed of lithium metaborate and lithium tetraborate, and the resulting mixture was fused into discs at 1200 °C. The discs were then analyzed using a Rigaku ZSX100e X-ray fluorescence (XRF) spectrometer with an analytical accuracy and precision of less than 1%. The concentration of major element in bulk sample was analyzed in TABLE S1. Subsequently, the major element concentrations were used to calculate the chemical index of alteration (CIA) as follows (Eq. (1)):

$$CIA = Al_2O_3/(Al_2O_3 + CaO + Na_2O + K_2O) \times 100\% \quad (1)$$

Trace element analysis

Powder samples were obtained from the drill core, dried at 105 °C for 3 h, and then baked at 550 °C for 3 h to remove organic material. Subsequently, approximately 0.04 g of each solid sample was dissolved in a mixture of hydrofluoric acid (HF), hydrochloric acid (HCl), and nitric acid (HNO_3) at 180 °C, and the trace element concentration in the resulting solution was analyzed using a Thermo Scientific iCAP Qc inductively coupled plasma–mass spectrometry (ICP-MS) system. Quantification was achieved by comparison against multi-element synthetic certified standard solutions and a rhodium standard solution, which served as the internal standard.

Accuracy and precision were greater than 3% for all of the analyzed elements.

Mössbauer spectral analysis

The ^{57}Fe Mössbauer spectra were collected at room temperature or 14 K using standard Mössbauer instrumentation (WissEL GmbH, Germany) equipped with a closed-cycle cryostat. The ^{57}Co in the rhodium matrix was used as a source of 14.4 keV gamma rays. Raw spectra were evaluated using MossWinn software. All of the spectra were calibrated against a standard absorber, which was 7-μm-thick α-Fe foil. The spectra were deconvoluted based on least-squares fitting of the Lorentzian line-shaped profile. The obtained sub-spectra attributable to different phases were classified on the basis of their hyperfine parameters, i.e., isomer shift (IS), quadrupole splitting (QS), and magnetic hyperfine field (B_{hf}). The proportion of each phase was determined by calculating the area of its corresponding sub-spectrum.

Scanning/transmission electron microscopy and EDX spectroscopy analysis

Micro-to-nanoscale observations of samples were performing by scanning electron microscopy (SEM) and transmission electron microscopy (TEM). Backscattered electron images of resin-impregnated polished thin sections were obtained using a Hitachi SU8010 SEM instrument operated at 15 kV. A sample was prepared for TEM and high-resolution TEM (HRTEM) by dispersion in ethanol, and a drop of the resulting suspension was then transferred onto a carbon-coated Cu grid, after which the ethanol was allowed to evaporate. Subsequently, TEM and HRTEM images of the dried sample

were obtained using an FEI Talos F200S instrument operated at 200 kV. Selected-area electron diffraction (SAED) patterns and fast Fourier transforms (FFTs) from high-resolution lattice-fringe images were analyzed to characterize mineral phases. EDS was performed using an energy-dispersive X-ray (EDX) detector operating in scanning transmission electron microscopy (STEM) mode.

Sequential extraction experiments

The following five-step sequential extraction method was used, based on a previous study (Ma et al., 2007).

Step 1: Ion-exchangeable portion of REEs. 1.0 g of a fine particulate sample was added to 40 mL of a 0.5 mol·L^{-1} solution of ammonium sulfate ($(NH_4)_2SO_4$) of pH 5, and the resulting suspension was continuously agitated for 10 h.

Step 2: Organic-associated portion of REEs. The solid residue from step 1 was added to 40 mL of a 0.1 mol·L^{-1} solution of sodium pyrophosphate of pH 10, and the resulting suspension was agitated for 10 h.

Step 3: Amorphous Fe (hydr)oxide-associated portion of REEs. The solid residue from step 2 was treated with 30 mL of a 0.25 mol·L^{-1} hydroxylamine hydrochloride ($NH_2OH{\cdot}HCl$) and 0.25 mol·L^{-1} HCl solution of pH 2, and the resulting suspension was heated in a water bath at 60 °C for 2 h.

Step 4: Crystalline Fe (hydr)oxide-associated portion of REEs. The residue from step 3 was treated with 40 mL of a 1 mol·L^{-1} $NH_2OH{\cdot}HCl$ and 25% acetic acid solution, and the resulting suspension was heated in a water bath at 90 °C for 3 h.

Step 5: Residual REE-bearing minerals. The solid residue from step 4 was washed twice with deionized water and then freeze-dried. The dried solid was added to a mixture of HCl, HNO_3, HF, and perchloric acid, and the resulting suspension was dissolved by heating at 200 °C for 3 h.

In each step, the supernatant was separated from the solids by centrifugation at 4000 rpm for 15 min. Subsequently, the supernatant was passed through a 0.22-μm filter, and the resulting filtrate was acidified with 1% v/v HNO_3 and then stored at 4 °C until elemental analysis on a Thermo Fisher iCAP Qc ICP-MS system. This revealed the REE concentrations in the supernatant, which were used to calculate the REE concentrations in each fraction. The solid residue was used in the next step of the extraction, as detailed above.

Synthesis of Fe (hydr)oxide and clay mineral composite

All of the chemicals and reagents were of analytical grade and used as received. The Fe (hydr)oxide and clay mineral composite was synthesized via a hydrothermal method (as detailed below) from biotite, which was collected from Lingshou County, Hebei Province, China. The composite was subsequently purified and then ground into a powder, and the chemical composition of the resulting powder was determined by XRF spectroscopy (TABLE S2).

The hydrothermal reaction was conducted as follows: Refined biotite samples (4.4 g L^{-1}) were added to a solution of 0.60 mol L^{-1} aluminum chloride ($AlCl_3$) hexahydrate (adjusted to a pH of 2 by addition of HCl) in a molar ratio of 1:100 in a Teflon vessel,

which was subsequently sealed in a stainless-steel autoclave and then heated at 150 °C for 60 days. Then, the autoclave was allowed to cool to room temperature and the precipitates were collected by centrifugation at 11,000 rpm for 10 min. The precipitates were washed three times with deionized water to remove residual $AlCl_3$ and were then freeze-dried. The resulting solid was labeled "Bt-60d".

REE adsorption experiment

REEs were adsorbed onto Bt-60d to simulate REE enrichment in a regolithic profile. The adsorption experiment was performed at 25 °C under atmospheric conditions in Teflon bottles to minimize retention of REEs by container walls. The suspension for each experiment was prepared by mixing 100 mg (M) of Bt-60 with 200 mL (V) of an REE solution containing 0–0.5 $mg \cdot L^{-1}$ of each lanthanide and Y, or 10 mg L^{-1} of neodymium (Nd) or ytterbium (Yb). The pH of each suspension was adjusted to by the addition of 0.1 mol L^{-1} HNO_3 or 0.1 mol L^{-1} NaOH, and the resulting suspension was agitated for 24 h until an equilibrium was established. The pH of each suspension was determined before and after the adsorption experiments, and the variation was found to be less than 0.25. Each adsorption experiment was performed three times using the same protocol to enable correction for experimental error. After adsorption, a solid sample was separated from the solution by centrifugation at 11,000 rpm for 20 min and subsequently analyzed by TEM–EDS analysis and REE desorption by $(NH_4)_2SO_4$. The supernatant was passed through a 0.22–μm filter, and the filtrate was acidified to pH by treatment with 1% v/v HNO_3. The resulting sample was analyzed by ICP-MS to an

accuracy and precision of better than 3%.

The adsorption concentration (q_e, $\mu g \cdot g^{-1}$) and adsorption coefficient (K_d, $mL \cdot g^{-1}$) were calculated by Eqs. (2) and (3), as follows:

$$q_e = (C_0 - C_e)V/m \quad (2)$$

$$K_d = (C_0/C_t - 1)V/M \quad (3)$$

where C_0 and C_t are the initial and equilibrium concentrations of REEs in solution, respectively.

The adsorption isotherms were fitted by a three-parameter Sips isotherm model that describes heterogeneous systems and is given by Eq. (4):

$$q_e = q_m K_s C_e^{ns}/(1 + KC_e^{ns}) \quad (4)$$

where q_m (mg/g) is the maximum adsorption concentration and K_s ($L^{ns}mg^{-ns}$) is the Sips isotherm constant; and ns is the Sips isotherm exponent, which ranges from −1 to +1. The Sips model becomes the Langmuir model when ns = 1 and becomes the Freundlich model at low C_0, and thus can represent most gas- or liquid-phase adsorption systems.

The Ce anomaly (δCe) was calculated using Eq. (5), as follows:

$$\delta Ce = C_{Ce}/[(C_{La} + C_{Pr})/2] \quad (5)$$

where C_{Ce}, C_{La}, and C_{Pr} are the concentrations of Ce, La, and Pr in each fraction after normalization to the concentration in parent rock, respectively.

RESULTS

Characteristics of the profile of the Renju deposit

From the top to down, the weathering profile of the Renju deposit can be divided into

four zones based on CIAs: a lateritic horizon (A horizon, 0–9 m, CIA > 90), a completely weathered horizon (B horizon, 9–59 m, CIA = 75–90), a semi-weathered horizon (C horizon, 59–85 m, CIA = 70–75), and a fresh bedrock (P horizon, 85–90 m, CIA < 70) (Figure 1). The thickness of the completely weathered horizon in the Renju deposit (50 m) is greater than the reported thicknesses of the weathering crusts in other typical deposits, e.g., the Zudong (6–30 m) (Li and Zhou, 2020), Dingnan (10 m) (Murakami and Ishihara, 2008), Zhaibei (12 m) (Borst et al., 2020), and Huashan (12.5 m) (Bao and Zhao, 2008) deposits in China; the Antsirabe deposit (13.5 m) in Madagascar (Ram et al., 2019); and the Phuket deposit (12 m) in Thailand (Sanematsu et al., 2013).

The bedrock is fine-grained (0.5–2.0 mm) equigranular quartz diorite (Figure S2a), composed mainly of plagioclase, hornblende, quartz, potassium feldspar (K-feldspar), biotite, and chlorite, with the latter being the hydrothermal alteration product of amphibole and biotite. REEs are primarily hosted in accessory minerals, such as allanite, titanite, apatite, xenotime, zircon, and monazite, with increasing weathering resistance. The C horizon is yellow-green (Figure S2b), owing to extensive chloritisation of biotite and hornblende. The protolith rock is decomposed, and fragments are widespread in weathered fractures. The lower B horizon is a mottled brownish-yellow (Figure S2c), whereas the upper B horizon is a mottled red and white and is less compact, probably due to the heterogeneous distribution of Fe (hydr)oxides in clay mineral aggregates (Figure S2d). Weathered quartz remnants were observed at the macroscopic scale. The A horizon is red and has a loose structure containing a few pores (Figure S2e). This

horizon is mainly composed of supergene minerals and contains some rounded residual quartz grains, but almost no primary feldspar or biotite.

With the increase of depth, the pH gradually increases from 4.3 at the topsoil to 7.3 in C horizon (Figure 1). The variation of weathering degree and pH greatly alters the distribution of main elements along the profile of the deposit. From the bottom up, the proportion of silica gradually increases, from 56.4% in the bedrock to 78.8% in the A horizon. In contrast, the proportion of alumina remains relatively stable, varying from 12.3% to 22.6%. Massive Fe (hydr)oxide particles are present in the upper B horizon, but the proportion of ferric oxide (Fe_2O_3) fluctuates along the profile of the deposit. For example, the proportion of Fe_2O_3 in the A horizon (3%) is higher than that in the upper B horizon (1%). This is ascribable to the weak acidic environment in the regolith, as this would contribute to the decomposition of minerals and the downward migration of more alkali metals and alkaline earth metals (e.g., potassium (K), sodium (Na), magnesium, and calcium (Ca)). In contrast, Fe is concentrated in the lower B horizon, with a maximum concentration of 11.8% at 54 m. This is probably ascribable to the abundance of Fe-bearing minerals with high weathering resistance (e.g., chlorite and biotite) in the bedrock, as these would not be affected by the initial stage of weathering. The variation in the concentration of manganese dioxide (MnO_2) was found to be similar to that of Fe_2O_3, but the concentration of MnO_2 is much lower than that of Fe_2O_3 (i.e., the Fe-to-Mn ratio is 10–100).

Regarding the distribution of REEs (Figures 1 and S3), it was found that the ∑REE concentration in bedrock is 496 ppm, which is markedly higher than the average ∑REE

concentration of granites in South China, i.e., 150–250 ppm (Li et al., 2017). The chondrite-normalized REE pattern is right-inclined and has an $(LREEs/HREEs)_N$ of 4.8, indicating the relative enrichment of LREEs over HREEs. In the C horizon, the ∑REE concentration and $(LREEs/HREEs)_N$ are near-constant, at 350 ppm and 4.0–4.6, respectively. In addition, the ∑REE concentration increases as the extent of weathering increases. For example, in the lower B horizon, there is a high ∑REE concentration (762 ppm) at 50 m, and the REE fractionation displays a slight HREE enrichment, as the $(LREEs/HREEs)_N$ is 1.1–2.7, which is lower than that of bedrock. In the upper B horizon (10–32 m), the ∑REE concentration rapidly increases and reaches a maximum (3343 ppm) at 16 m that is ca. 6.6 fold higher than that in the bedrock. Moreover, in this horizon, there is a substantial accumulation of LREEs and the $(LREEs/HREEs)_N$ (5.0–17.8) is much larger than that of bedrock (4.8). In the A horizon, the ∑REE concentration decreases to 350–550 ppm, close to that of parent rock. However, unlike in bedrock, the REEs in this horizon are dominated by Ce, due to a strong positive Ce anomaly, resulting in a high $(LREEs/HREEs)_N$ (14.0). Thus, in the Renju profile, LREEs and HREEs are concentrated in the upper and lower B horizon, respectively, while Ce is enriched in the topsoil. These distribution characteristics are identical to those of other typical deposits, e.g., the Zudong (Li et al., 2017) and Longnan deposits (Bao and Zhao, 2008) in Jiangxi Province, China.

The bulk sample was divided into three fractions based on particle size: a fine particle (< 2 μm) fraction, a medium particle (2–20 μm) fraction, and a large particle (>20 μm) fraction. Generally, the proportion of the fine-particle fraction increased from the

bottom to the top of the soil profile (Figure 2a). In the C horizon (e.g., 66 m), the fine and large particle fractions comprised ca. 7% and 65% of the soil profile, respectively. As the weathering degree increased, the proportion of the fine particle fraction gradually increased, reaching 15%–35% in the B horizon and more than 40% in the A horizon. In contrast, the proportion of large particle fraction steadily decreased as the degree of weathering increased, reaching less than 5% in the A horizon. An analogous trend was recently identified in the Zudong deposit (Li and Zhou, 2020).

In the current study, although the fine particle fraction was not predominant, its contribution to REE enrichment was equal to or greater than that of the large particle fraction. That is, in the A and upper B horizons (at depths of 2–20 m), the concentrations of REEs in the fine particle fraction were comparable to those in the large particle fraction (Figure 2b). Moreover, at greater depths (20–66 m), i.e., in the lower B and C horizons, there was less of the fine particle fraction than of the other fractions, but REEs were preferentially enriched in the fine particle fraction. For example, at 36 m, approximately 88% of REEs were present in the fine particle fraction. Thus, given the vital role of fine particles in REE mineralization, the fine particle fraction was extracted to allow an in-depth investigation of its mineral composition, surface physicochemical properties, and REE distribution.

Mineral composition

XRD

The main mineral phases were identified from the diffraction positions and intensities

in the XRD patterns of bulk samples (Figure S4). In the weathering crust, kaolinite (or halloysite-7Å), quartz, and orthoclase were found to be the dominant minerals, as they accounted for more than 70% of the mineral composition. In addition, their distribution changes with the degree of weathering. Kaolinite and halloysite are predominant in the A and upper B horizons (25%–50%), while orthoclase, a rock-forming mineral is enriched in the lower part of the B horizon (25%–55%). In contrast, quartz is a mineral resistant to weathering and is thus present in the same proportion across the whole profile. The minor components detected include illite, muscovite, and plagioclase, but these are rock-forming minerals or intermediate weathering products, and therefore present only at the bottom of the B horizon such as at 55 m in Figure S4.

Compared with the bulk sample, the fine particle fraction (<2 μm) was found to contain more clay minerals and thus have more defined XRD patterns (Figure 3a). Similar to the bulk samples, kaolinite and/or halloysite-7Å prevail along the profile of the deposit, with characteristic (001), (020), and (002) reflections at ca. 7.17, 4.47, and 3.58 Å, respectively. Therefore, oriented samples before and after the intercalation of formamide or ethylene glycol were investigated to determine the clay minerals that were present (Figure 4). This was done as the preparation of oriented samples can reveal the preferential orientation of clay minerals, since it enhances the intensity of characteristic (001) reflections. Specifically, intercalation of formamide can distinguish halloysite-7Å from kaolinite, as they have interlayer spacings in the range of 10–11 Å and ca. 7 Å, respectively. Similarly, intercalation of ethylene glycol increases the interlayer spacing of swelling clay minerals, which is revealed by the shifting of the

(001) diffraction to a low angle. This allows montmorillonite (a swelling clay mineral) to be distinguished from chlorite (a non-swelling clay mineral). The XRD patterns of oriented samples of all of the fine particle fractions except for that collected from the C horizon (i.e., at 65 m) resembled those with ethylene glycol intercalation, thereby demonstrating that swelling clay minerals are absent at most depths in the deposit.

By means of the aforementioned treatments, the mineral composition of the fine particle fraction was resolved (Figure 4). In topsoil (e.g., at 2 m), the patterns of oriented samples without and with formamide intercalation, respectively, exhibited no diffractions at 10 Å. This shows that in topsoil, halloysite-7Å is not present, whereas kaolinite, which could not be determined in the bulk sample, is predominant. With increasing depth (i.e., at 6–20 m), both halloysite-7Å and kaolinite are present, as there is a diffraction at ca. 10 Å in the patterns of formamide-intercalated samples but not in those of non-formamide-intercalated samples. With a further increase in depth (i.e., 28–48 m), the patterns of oriented samples exhibited an unambiguous diffraction at ca. 10 Å, which is attributable to the (001) reflection of illite. Moreover, the reflections at ca. 5.02 and 4.48 Å correspond to characteristic (004) and (110) reflections of illite, respectively. Interestingly, compared with the air-dried oriented samples, the intensity of the diffractions of the formamide-intercalated samples was slightly stronger, suggesting the presence of a small amount of halloysite. Thus, the clay minerals at 28–48 m are mainly kaolinite, halloysite, and illite. The diffraction at ca. 10 Å was also present in the patterns of air-dry oriented samples from the C horizon (e.g., at 55–65 m), and its intensity was comparable to that in the patterns of formamide-intercalated

483 samples, which shows that halloysite is not present in the C horizon. This diffraction is
484 attributable to the (001) reflection of muscovite. Additionally, there were characteristic
485 (002) and (-112) reflections of muscovite at ca. 4.95 and 3.62 Å, respectively (Figure
486 3a), and there is clearly more of this mineral in the C horizon than at 28–48 m. That is,
487 tiny lamellar-structured and weakly orientated illite is dominant at 28–48 m, whereas
488 intact lamellar-structured and strongly oriented muscovite is dominant at 55–65 m.
489 Taken together with the 7 Å diffraction, which is assignable to kaolinite, these results
490 show that the clay minerals in the C horizon are mainly kaolinite and muscovite.
491 Additionally, a small amount of montmorillonite was detected in the powder XRD
492 pattern of a sample from 65 m, as indicated by the (001) diffraction at 15 Å. However,
493 this diffraction was not present in the pattern of intercalated or non-intercalated samples,
494 which is probably ascribable to a low concentration of lowly crystalline
495 montmorillonite being present.

496 Based on the XRD patterns and aforementioned phase identification, the clay mineral
497 composition in fine particle fraction is obtained (Figure 3b). The variation in the
498 composition was identical to that in the bulk sample. Specifically, in the C horizon,
499 kaolinite and muscovite account for 45%–55% and 10%–35% of the composition,
500 respectively. At greater depths (i.e., at 28–48 m), muscovite is absent, whereas
501 halloysite and illite are present, with the proportion of kaolinite being greatly enhanced
502 (ca. 70%) and higher than those of halloysite (<35%) and illite (<25%). In contrast, at
503 depths subjected to increased weathering (at 6–20 m), illite disappears, and the contents
504 of kaolinite and halloysite fluctuate in the range of 45%–70% and 30%–55%,

505 respectively. In the topsoil, kaolinite is the predominant clay mineral (95%). Compared
506 with the proportions of quartz and orthoclase in the bulk sample, those in the fine
507 particle fraction are significantly lower (<10% and <5%, respectively).
508
509 Mössbauer spectroscopy
510 Interestingly, XRD effectively distinguished the phases of clay minerals but failed to
511 detect Fe (hydr)oxides, even in samples from depths at which the Fe (hydr)oxide
512 proportion is up to 10%. Thus, ^{57}Fe Mössbauer spectroscopy was used to analyze
513 samples of the fine particle fraction to investigate the variation in the crystallinity and
514 composition of Fe-bearing minerals. All of the spectra collected at room temperature
515 (RT, i.e., 298 K) contained a doublet overlapping one or two small sextets (Figure S5
516 and TABLE S3). The doublet had an IS value of 0.36 mm s^{-1}, which is consistent with
517 ferric ion (Fe(III))-bearing species, such as Fe(III) aluminosilicates and Fe(III)-
518 (hydr)oxides, which are super-paramagnetic (SP) at RT but could not be distinguished
519 at RT. Along the profile of the deposit, these species host more than 69% of the total Fe.
520 The sextets may be attributable to hematite and goethite, as they have negative QS
521 values similar to those minerals (i.e., -0.19 to -0.25 mm s^{-1} for hematite and -0.20 to -
522 0.26 mm s^{-1} for goethite). However, the B_{hf} of hematite (49.0–51.0 T) is larger than that
523 of goethite (31.0–31.4 T). Hematite and goethite sextets appeared in the spectra of
524 samples from depths above 16 m and 28–36 m, in proportions of 19%–33% and 22%–
525 31%, respectively. The small size of these sextets in the spectra is indicative of a small
526 proportion of highly crystalline hematite and goethite present in the fine particle

fraction. This accounts for the non-detection of Fe (hydr)oxide minerals by XRD. In addition, the small sextets were absent from samples from depths below 48 m. This is probably due to the fact that at these depths, the Fe(III)-bearing species exist as less crystalline Fe(III)-(hydr)oxides or as Fe(III) in aluminosilicates. In addition, there was a doublet with an IS of 1.14 mm s^{-1} in the spectrum of a sample from a depth of 65 m, corresponding to a ferrous-ion (Fe(II))-bearing species. Based on the lithology of the bedrock, this Fe(II)-bearing species is primarily attributable to octahedral Fe(II) in biotite.

Cooling the samples to 14 K generated sextets with increased areas, and a doublet, as most Fe(III)-(hydr)oxides are magnetically ordered (Figure S6 and TABLE S4). The Fe(III) sextets were highly similar to those of hematite, goethite, or ferrihydrite. Compared with the hematite sextet detected at RT, that detected at 14 K had a larger IS (0.43–0.48 mm s^{-1}), QS (-0.25 to -0.16 mm s^{-1}), and B_{hf} (49.7–51.2 T), although this QS value is lower than the classical value reported by Cornell and Schwertmann (1996). Schwertmann et al. (2000) attributed this phenomenon to Al substitution in hematite, which is a rather common occurrence in soils. As the depth decreased, the QS value gradually increased, from -0.25 mm s^{-1} (at 28 m) to -0.16 mm s^{-1} (at 2 m). This is probably related to the decrease in Al substitution in hematite, due to the re-crystallization of Fe (hydr)oxides during weathering (Cornell and Schwertmann, 1996). Moreover, spectra obtained at 14 K revealed the presence of hematite not only in topsoil and the upper B horizon (0–16 m), which is accordance with RT spectra, but also in the middle part of the B horizon (16–28 m), suggesting the presence of nanoparticulate or

549 lowly crystalline hematite. Overall, the results show that hematite hosts 53%–88% of
550 the total Fe, with its proportion of this total decreasing with depth (Figure 5).

551 The IS (0.43–0.52 mm s^{-1}) and QS (-0.32 to -0.20 mm s^{-1}) of goethite are identical to
552 those of hematite, but the B_{hf} of goethite (46.9–51.3 T) is lower than that of hematite
553 and close to those reported for a goethite standard (Cornell and Schwertmann, 1996).
554 The 14 K spectra demonstrated that goethite is prevalent in the entire B horizon and
555 upper C horizon (28–55 m), whereas the RT spectra demonstrated that goethite is
556 present in only part of the aforementioned area (28–36 m). This illustrates that goethite
557 also exists in the C horizon in a nanoparticulate or amorphous form. Thus, hematite is
558 enriched in the upper part, whereas goethite is enriched in the lower part (i.e., in
559 proportions of >45% at 28–55 m). In addition, the B_{hf} of goethite decreases as the depth
560 decreases, implying that there is a reduction in magnetism at shallower depths. This is
561 ascribable to the fact that increased weathering not only decreases the crystallinity of
562 goethite but also increases the substitution of Fe by Al and other elements.

563 A sample collected from a depth of 28 m had no sextet for ferrihydrite in a spectrum
564 obtained at RT, but did have such a sextet in a spectrum obtained at 14 K, due to
565 magnetic ordering, with an IS of 0.36 mm s^{-1}, a QS of 0.04 mm s^{-1}, and a B_{hf} of 54.2 T.
566 Thus, it was found that ferrihydrite hosts 8% of the total amount of Fe. This is because
567 ferrihydrite is the precursor for most Fe (hydr)oxides in soil, as it is metastable and
568 contains rather small crystallites. Moreover, due to its large surface area, ferrihydrite
569 can be complexed with organic matter (OM), such that it appeared as a doublet in a
570 spectrum obtained at RT but as a sextet with a QS close to 0 in a spectrum obtained at

14 K (Van Ranst et al., 2019). Compared with the spectrum obtained at RT, the contribution of the doublet was substantially decreased (7%–43%) in the spectrum obtained at 14 K, although it was detectable in the spectra of all of the samples. The IS was 0.37–0.44 mm s^{-1}, while the QS was 0.52–0.78 mm s^{-1}. At 14 K, most of the Fe(III) (hydr)oxides were magnetically ordered, and thus this sub-spectral pattern is attributable mainly to Fe(III) complexed to OM or within non-Fe-rich silicates. For example, Fe(III) ions in aluminosilicates are too distant from each other to order magnetically and thus are present as a doublet at 14 K (Chen et al., 2019). Additionally, a special doublet with an IS of 0.80 mm s^{-1} and a QS of 2.22 mm s^{-1} was present in the spectrum of a sample collected from a depth of 2 m, and is probably attributable to an Fe(III)–Fe(II) species complexed with OM in the humid soil environment (Robic et al., 2022). Consistent with the spectrum obtained at RT, Fe(II)-bearing species with an IS of 1.31 mm s^{-1} and a QS of 2.27 mm s^{-1} were detected in the spectrum obtained at 14 K of a sample collected from 65 m. This is attributable to the small proportion (ca. 5%) of Fe(II) originating from biotite in the C horizon.

SEM and TEM observations

The SEM images (Figure 6) showed that clay minerals and Fe (hydr)oxides co-exist and form composites in each horizon. Most clay minerals are micro-sized lamellar particles ranging from a few micrometers to nanometers in thickness. Fe (hydr)oxides generally form nano-sized particles that are much smaller than clay mineral species. Therefore, most Fe (hydr)oxide particles are attached to the basal surface of clay minerals, with only a few adhered to the edge of clay minerals.

The morphologies and phase compositions of clay–Fe (hydr)oxide composites from different horizons were further investigated by TEM. In the C horizon (Figures 6d and 7), kaolinite and muscovite are the main clay minerals, which is in line with the XRD results. Both of these clay minerals have a typical lamellar morphology, with dominant (001) crystal planes. They are distinguished by their chemical composition, as the silicon-to-aluminum (Si-to-Al) ratios of kaolinite and muscovite are close to 1 and larger than 1, respectively. Moreover, kaolinite is devoid of K, whereas muscovite contains 3%–4% K, as detected by EDS analysis. Muscovite is a common rock-forming mineral that has a crystal structure and elemental composition similar to those of illite but contains more K than illite. The HRTEM image showed that it has a euhedral plate-like crystal shape and lattice fringes. Most kaolinite particles occur as irregular slices randomly stacked around fractured flake-like muscovite particles that are 0.5–3.2, 0.2–0.6, and 0.2–0.5 μm in length, width, and thickness, respectively. In addition, ferrihydrite and goethite were found to be present. Ferrihydrite forms micron-sized aggregates, which were readily identified in TEM images. Consistent with the Mössbauer results, ferrihydrite is poorly crystallized, as its SAED pattern shows diffraction rings with *d*-spacings of 0.15 and 0.26 nm, corresponding to the (115) and (110) planes, respectively. Goethite is present as nano-sized particles in the cavities of ferrihydrite aggregates and has diffraction rings with *d*-spacings of 0.49 and 0.25 nm, corresponding to the (020) and (021) planes, respectively.

In the lower B horizon (Figure 6c and 8), it was found that muscovite is absent, whereas illite is present. The SEM image showed that a small quantity of kaolinite

616 particles are present, either as thin "booklets", thin-sheet agglomerates, or irregularly
617 layered stacks. Halloysite particles are short (generally less than 0.5 μm) and distributed
618 around kaolinite and illite. Most particles appear as tubular stacks that form disorderly
619 aggregates. Illite grains form lumpy particles that are 0.7–2.0 μm in length and 0.4–1.2
620 μm in width. EDS revealed that illite contains 1%–2% K, with a Si-to-Al ratio of ca. 2.
621 In the HRTEM image, illite exhibited lattice fringes with a periodicity of 10 Å on the
622 crimped edge (Figure 8b). Kaolinite is obviously larger, with a length, width, and
623 thickness of 1–2, 0.5–1 and 0.5–1 μm, respectively (Figure 8a). Consistent with the
624 Mössbauer results, goethite and ferrihydrite are present and form composites, but
625 ferrihydrite remains poorly crystallized and present in a much lower proportion than in
626 the C horizon. Thus, goethite is the dominant Fe (hydr)oxide. In addition, compared
627 with the C horizon, goethite exhibits greatly increased crystallinity and thus forms near-
628 acicular crystals with lengths of up to 200–400 nm. Therefore, goethite particles form
629 long strip-shaped aggregates that attach to the edge of kaolinite (Figure 8c).
630 Interestingly, the edge of goethite and ferrihydrite composites are amorphized, which
631 is attributable to the dissolution of ferrihydrite and recrystallization of goethite. This
632 also explains their variation in concentration (Figure 8d).

633 In the upper B horizon, additional weathering (Figure 6b and 9) results in "booklet"
634 kaolinite becoming more abundant and larger (thicknesses of 1.5–2.2 μm) than in the
635 lower B horizon, whereas illite is absent (Figure 9a). Moreover, two forms of halloysite
636 are present: long (3.0–5.0-μm) and smooth tubes that are individually attached to the
637 kaolinite surface (Figure 6b), and nanotubular particles (internal diameters of ca 10–30

nm and lengths of 50–200 nm) that are mostly attached to the base or edges of kaolinite with semi-unfolded shapes (Figure 9b). Goethite is present as composites with kaolinite that are long and acicular, but their particle size significantly decreases to 100–300 nm (Figure 9d). In addition, hematite was identified by its SAED pattern: *d*-spacings of 0.36 and 0.25 nm, corresponding to the (012) and (-1-10) planes, respectively. The hematite particles exist as nanocrystal aggregates that are 20–50 nm in size (Figure 9c).

In the A horizon, which is subject to intensive weathering, the "booklet" kaolinite form is much thicker than that in the B horizon (Figure 6a and 10). In addition, vermicular kaolinite was found in the bulk sample. Halloysite is mostly present as 1–5-μm long and fine tubes (Figure 6a). The XRD analysis revealed that this is mainly 7Å-halloysite. Hematite is also highly crystalline and present as particles with greater sizes (tens of nanometers) than those in the lower horizons. These hematite particles stack to form aggregates that are widespread on the surfaces or along the edges of kaolinite (Figure 10a-c).

REE speciation

Sequential extraction enabled REEs to be identified in an ion-exchangeable state, an organic-associated state, an Fe–Mn (hydr)oxide-associated state, and a residual REE-bearing mineral state. In the fine particle fraction, ion-exchangeable and Fe–Mn (hydr)oxide associated states account for more than 90% of the total REEs (Figure 11). This is due to the ubiquity of clay minerals and Fe (hydr)oxides, and the deficiency of REE-bearing minerals observed in TEM. Organic-associated REEs comprised the

660 smallest proportion of REEs in the A and B horizons (<5%), due to the low
661 concentration of organic carbon in the profile of the deposit (0.03%–0.2%). Thus, the
662 distribution and fractionation characteristics of ion-exchangeable and Fe–Mn
663 (hydr)oxide associated REEs were the focus of this investigation. As the concentration
664 of Fe is much higher than that of Mn (Figure 1g, h), there were no Mn (hydr)oxides
665 detected in TEM observations, and thus REEs are likely bonded to Fe (hydr)oxides
666 rather than to Mn (hydr)oxides.

667 Along the profile of the deposit, ion-exchangeable REEs are almost invariably
668 dominant, in proportions of greater than 70%, except in the A horizon, where the
669 proportions are ca. 25% at 2 m (Figure 11), and in the C horizon, where the proportions
670 are ca. 8% and 50% at 55 and 65 m, respectively. As the extent of weathering increases,
671 the proportions of ion-exchangeable REEs initially increase and then decrease. REEs
672 bound to Fe (hydr)oxides are enriched in the A (a proportion of 70%) and C horizons
673 (proportions of 50% and 90%). They are also present in the B horizon but in much
674 smaller proportions (<20%) than the ion-exchangeable REEs. Sequential extraction
675 enabled them to be divided into two portions: a portion bonded to amorphous Fe
676 (hydr)oxides, and a portion bonded to crystalline Fe (hydr)oxides. At most sampling
677 sites, the proportion of the former state (mostly >15%) is significantly higher than the
678 latter state (mostly <8%).

679 The parent rock and entire weathering profile are generally enriched in LREEs, but
680 the aforementioned REE species are clearly fractionated into LREEs and HREEs
681 (Figure S7). In addition, there is a substantial Ce anomaly: Ce is deficient in the ion-

682 exchangeable state (in the A and B horizons), but concentrated in the Fe (hydr)oxide-
683 associated state (in the A, B, and C horizons), respectively. To eliminate the influence
684 of the Ce anomaly, the fractionation into LREEs and HREEs was discriminated by
685 determining (LREE-Ce)/$HREE_{s/p}$ values (Text S1), which represent the LREE-Ce-to-
686 HREE ratio of a specific state vs. that of parent rock. In ion-exchangeable REEs, the
687 parent rock-normalized REE pattern is right-inclined in the A and upper B horizons
688 (Figure S7.a), with (LREE-Ce)/$HREE_{s/p}$ values of 1.61, 3.83, and 2.87 at the 2, 10, and
689 16 m, respectively (Figure 12a), suggesting that these depths are enriched in LREEs.
690 However, as the depth increases, the ion-exchangeable state preferentially scavenges
691 HREEs, as the patterns change to be left-inclined (Figure S7.b and S7.c), and the
692 (LREE-Ce)/$HREE_{s/p}$ values gradually approach ca. 0.5 in the lower B and C horizons.
693 In amorphous Fe (hydr)oxide-associated REEs, the variation in the fractionation
694 patterns is identical to that in the ion-exchangeable REEs, but is left-inclined at most
695 depths (Figure S7d–S7f). At 2–16 m, the (LREE-Ce)/$HREE_{s/p}$ values (0.64–1.92) are
696 clearly lower than those of ion-exchangeable REEs (0.38–3.83). With increasing depth,
697 these values first decrease to ca. 0.50 and then gradually approach 1 in the C horizon.
698 Conversely, the patterns of crystalline Fe (hydr)oxide-associated REEs are left-inclined
699 across the entire profile (Figure S7g–S7i), and their (LREE-Ce)/$HREE_{s/p}$ values remain
700 below 1 and generally below 0.50.
701 The variation in (LREE-Ce)/$HREE_{s/p}$ values illustrates that in both ion-exchangeable
702 and Fe (hydr)oxide-associated REEs, HREEs are enriched in deeper horizons than
703 LREEs. To further explore this impact, fractionation into LREEs and HREEs was

discriminated by determining (LREE-Ce)/$HREE_{s/w}$ values (Figure 12b), which represent the ratio of LREE-Ce-to-HREE for a specific state vs. that of whole rock at the same depth (Figure 1c). This enabled a comparison of the ability of clay minerals and Fe (hydr)oxides to selectively bind LREEs and HREEs, respectively. The (LREE-Ce)/$HREE_{s/w}$ values for ion-exchangeable REEs at most depths are approximately 1 (1.05–1.15), suggesting that clay minerals non-selectively adsorb these REEs. In contrast, the (LREE-Ce)/$HREE_{s/w}$ values of crystalline and amorphous Fe (hydr)oxide-binding REEs are mostly less than 1, but those of the former are significantly lower (mostly < 0.5) than those of the latter (0.49–0.82). This indicates that crystalline Fe (hydr)oxide-binding REEs selectively adsorb HREEs rather than LREEs.

Adsorption experiment

A clay–Fe (hydr)oxide composite was prepared through the hydrothermal transformation of biotite to further examine the contribution of Fe (hydr)oxides and clay minerals to the enrichment and fractionation of REEs. The obtained product (Bt-60d) contained clay minerals: predominantly kaolinite, together with Fe (hydr)oxides such as goethite and hematite (Figure S8–S10, TABLE S5). The mineral composition was identical to that of the fine particle fraction at 28 m, which is located in the upper B horizon with the highest REE enrichment. Thus, Bt-60d was used in the adsorption experiment to simulate REE enrichment in weathering crust.

Considering that pH varies along the weathering profile, REEs were adsorbed onto Bt-60d at pH 6, which is similar to the pH measured at 28 m (Figure 1b). The adsorption

726 isotherms were well fitted by the Sips adsorption model (Figure 13a, coefficient of
727 determination = 0.99), which is a hybrid of the Langmuir and Freundlich models (Wang
728 and Guo, 2020) that is based on the assumption that monolayer REE adsorption occurs
729 at more than one active site. The adsorption capacities of Bt-60d for Nd and Yb were
730 calculated to be 0.64 and 0.69 mg g^{-1}, respectively.

731 Bt-60d was further used to adsorb REEs at the initial concentration of 0.20 mg L^{-1}
732 for each REE. The total adsorbed concentration of REEs was ca. 4000 μg g^{-1} (Figure
733 13), which is similar to the REE concentration in the fine particle fraction at 28 m
734 (Figure 2). The log K_d of adsorbed REEs is similar throughout the REE group (Figure
735 13). This is consistent with the fact that the adsorption capacities of Bt-60d for Nd and
736 Yb are similar. Sequential extraction enabled the enrichment pattern of REEs in
737 different fractions to be clarified (Figure 13a). For ion-exchangeable REEs, the pattern
738 is nearly flat, with an (LREE-Ce)/HREE of 1.01, whereas those of amorphous and
739 crystalline Fe (hydr)oxide-associated REEs are weakly and markedly left-inclined, with
740 (LREE-Ce)/HREE values of 0.68 and 0.48, respectively. These fractionation
741 characteristics are identical to those of the same species of REEs detected at 28 m, as
742 shown by the (LREE-Ce)/$HREE_{s/w}$ values of 0.99, 0.84, and 0.74 for ion-exchangeable,
743 amorphous, and crystalline Fe (hydr)oxide-associated REEs, respectively. Interestingly,
744 there was no Ce anomaly in any REE state in Bt-60d. This is different from the situation
745 at a depth of 28 m, where ion-exchangeable REEs display a negative Ce anomaly (δCe
746 = 0.004), whereas amorphous and crystalline Fe (hydr)oxide-associated REEs show a
747 positive Ce anomaly (δCe = 12.9 and 9.08, respectively).

748 The distribution of LREEs and HREEs on Bt-60d was also observed by TEM-EDS.
749 Nd and Yb were selected as the representative LREE and HREE, respectively, and
750 individually adsorbed onto Bt-60d. In the EDS maps of this Fe (hydr)oxide–clay
751 mineral composite (Figures 14a, d and 15a, d), Fe overlaps Al (Figures 14b, e and 15b,
752 e), with these being characteristic elements of Fe (hydr)oxides and clay minerals,
753 respectively. This indicates that the Fe (hydr)oxide particles were attached onto the
754 surfaces of the clay minerals.

755 Nd was found to be uniformly dispersed, as in most composites with Fe-to-Al mass
756 ratios of 0.32–2.19, the concentration of Nd was 0.67%–0.90% (Figure 14b, c, e and f).
757 $(NH_4)_2SO_4$ is a typical lixiviant that is used to extract ion-exchangeable REEs, and after
758 REE desorption by treatment with $(NH_4)_2SO_4$, the Nd concentration greatly decreased.
759 For instance, in the region representing composites with an Fe-to-Al ratio of 0.52, the
760 concentration of Nd was less than 0.14% (Figure 14h–14i). Conversely, Yb was less
761 homogeneously distributed and appeared to be more closely associated with Fe than Al.
762 For example, in the composite with an Fe-to-Al ratio of 0.21, the proportion of Yb was
763 1.47% (Figure 15e, f), whereas in that with an Fe-to-Al ratio of 13.6 (i.e., containing
764 more Fe (hydr)oxides, the proportion of Yb was higher, i.e., 5.54% (Figure 15b, c). This
765 verifies that Fe (hydr)oxide minerals are selectively enriched in HREEs (Ohta et al.,
766 2009b). After extraction by $(NH_4)_2SO_4$, the proportion of Yb was also significantly
767 decreased, e.g., 1.05% remained in the composite with an Fe-to-Al ratio of 5.58.
768 However, the proportion remained high (3.45%) in the region rich in Fe, i.e., with an
769 Fe-to-Al ratio of 179.9 (Figure 15h, i). This indicates that REEs bound to Fe

770 (hydr)oxides are more stable than REEs bound to other species.

771

DISCUSSION

Chemical weathering is preferentially promoted by temperate and tropical climatic conditions, but the thickness of weathering crust is determined by the equilibrium between weathering and denudation processes. Previous studies suggest that ion-adsorption-type REE deposits are mainly located in temperate or tropical regions, where thick weathering crusts are well preserved (Li et al., 2017; Yaraghi et al., 2020). Thus far, subtropical weathering of granite in South China has led to the formation of numerous ion-adsorption-type REE deposits. For example, in the Renju deposit in South China, a thick weathering crust up to 85 m deep has developed and exhibits dramatic variations in geochemistry and mineralogy with depth. This is resulted from the weathering of parent rock, accumulation of residual primary minerals and generation of secondary minerals.

The dissolution of REEs from bedrock into leachate is the basis of deposit formation, which depends on the weathering resistance of REE-bearing minerals. Thus, the patterns of REEs in the weathering crust are largely inherited from those of parent rocks (Figure S3). During downward eluviation, REE ions are complexed with humic substances and carbonates or REE(III) ions and migrate downwards, and HREEs bond more strongly than LREEs to the aforementioned ligands and thus are transported deeper than LREEs (Ohta et al., 2009b). Hence, LREEs and HREEs are concentrated in the upper and lower parts of weathering crust, respectively (Figure 12a). Subsequently, REE anions are adsorbed by secondary minerals. Moreover, the phases and morphologies of these minerals vary with the extent of weathering, especially those

of clay minerals and Fe (hydr)oxides, which are the major carriers of REE ions.

Variation in clay minerals

Warm and humid climatic conditions accelerate the dissolution of rock-forming minerals (White et al., 2001). This gives rise to the leaching of most mobile elements (e.g., K, Na, and Ca), whereas residual elements (e.g., Al, Si, Fe, and titanium) form clay minerals. In the weathering crust, the variation of geochemical conditions (e.g., pH, fluid activity, and ionic strength) with depth causes the evolution of clay minerals, resulting in the variation of clay mineral concentrations with depth.

In the parent rock of the Renju deposit, the primary rock-forming minerals are primary chlorite, hornblende, biotite, plagioclase, orthoclase, and quartz, with different degrees of weathering resistance (Bao and Zhao, 2008). This determines their order of disappearance within the weathering crust. In the semi-weathered horizon, which represents an incipient stage of weathering, plagioclase, orthoclase, and quartz are preserved, as they have a high weathering resistance; in particular, quartz is barely decomposed and persists across the entire profile (Figure 3). In contrast, chlorite, hornblende, and biotite are completely decomposed, as they have low weathering resistance, and this is accompanied by the emergence of muscovite, montmorillonite, and kaolinite. Muscovite is the weathering product of plagioclase; thus, its concentration increases as that of plagioclase decreases. Analogously, montmorillonite is formed by the decomposition of orthoclase and plagioclase, but is unstable and thus only transitorily retained in this layer. The formation of montmorillonite features the

816 transformation of a framework silicate into a layered silicate via a dissolution–
817 recrystallization mechanism (Wilson, 2004). Initially, orthoclase and plagioclase are
818 dissolved along micro-cracks and bi-crystal planes to form a protocrystalline
819 intermediate containing polymers inherited from the bulk structure. This intermediate
820 then crystallizes to form montmorillonite, which requires most structural Al to change
821 from a four-coordinate to a six-coordinate form, the rearrangement of tetrahedral and
822 octahedral units, the precipitation of cations (e.g., K and Na), and the addition of
823 hydroxyl groups and water molecules (Banfield and Eggleton, 1990). Compared with
824 muscovite and montmorillonite, kaolinite originates from more species and thus is
825 present in higher concentrations. The mineral composition in parent rock suggests that
826 the formation pathways of kaolinite are (i) plagioclase → muscovite → halloysite →
827 vermicular kaolinite; (ii) plagioclase → muscovite → microcrystalline kaolinite →
828 vermicular kaolinite; (iii) biotite → vermiculite →
829 montmorillonite/illite/chlorite/mixed-layered mineral → kaolinite; (iv) orthoclase →
830 montmorillonite + illite → kaolinite + halloysite; and (v) orthoclase → halloysite →
831 kaolinite (Jeong, 1998; Papoulis et al., 2004). The above transformation pathways of
832 clay minerals are also found in the weathering of other type of granite (Bao and Zhao,
833 2008).

834 Several possible intermediate products, e.g., illite and halloysite, are absent but
835 emerge in the upper part of the weathering crust. This indicates that kaolinite is largely
836 generated from muscovite. In contrast to kaolinite on completely weathered layers,
837 which has a thick “booklet” morphology and large particle sizes (> 1 μm), kaolinite in

838 semi-weathered layer displays a fragmented shape with a microcrystalline size (< 1 μm).
839 This is because a low degree of weathering means that decomposition of primary
840 minerals occurs only in confined spaces, e.g., micro-cracks and cleavage joints of
841 minerals, leading to a small particle size. This also suggests that the transformation of
842 muscovite into kaolinite is a topotactic alteration (Singh and Gilkes, 1991).

843 In the lower part of the completely weathered layer, eluviation–illuviation processes
844 and local groundwater flows are intensified, resulting in an increase in intergranular
845 cracks and cleavage, and in the porosity and SSA of minerals. Thus, this layer is
846 exposed to the environment and its rocks are extensively affected by water. Under these
847 conditions, rock-formation minerals are substantially affected: muscovite is entirely
848 decomposed, and the concentration of orthoclase significantly decreases (Figure 3).
849 Secondary minerals are also affected: montmorillonite is entirely decomposed, and this
850 is accompanied by accumulation of illite and halloysite (Dill et al., 2016). The
851 transformation pathways suggest that illite is formed via the weathering of orthoclase
852 and muscovite, which provide sufficient K. However, illite is only present in this layer
853 and its concentration decreases as the depth decreases. The decomposition of illite
854 follows a dissolution–precipitation mechanism, leading to removal of K and Na from
855 the interlayer, and thus local supersaturation of Si and Al, resulting in the transformation
856 of illite to 1:1 clay minerals with a more stable structure (e.g., kaolinite and halloysite)
857 (Li and Zhou, 2020; Li et al., 2020a). For example, in a water-saturated environment, a
858 misfit of octahedral sheets with tetrahedral sheets is offset by the rolling and
859 incorporation of interlayer water molecules to form halloysite-10 Å (Yuan et al., 2015).

Thus, the concentration of halloysite is negatively correlated with that of illite (Figure 3). The incipient halloysite exhibits a short and stubby morphology (Figure 6), but in the upper part of the completely weathered layer it gradually changes into a long and tubular morphology. Semi-unfolded halloysite is also present, in close association with kaolinite. Fluctuation in the height of the water table leads to alternating wet and dry conditions in this layer, which results in removal of interlayer water. This causes the tubular morphology to unfold and then transform into kaolinite (Yuan et al., 2012). Compared with the kaolinite in the semi-weathered layer, most of the kaolinite in the lower part of the completely weathered layer has an identical morphology but a larger particle size.

In the topsoil, vigorous biological activity and the presence of atmospheric water cause intense chemical and biological weathering. Repeated wetting and drying episodes irreversibly dehydrate metastable halloysite-10 Å into halloysite-7 Å (Inoue et al., 2012). Most halloysite-7 Å has a thin and long (1–5 μm) tubular structure (Figure 6). With prolonged dehydration, these tubes unroll and are transformed into kaolinite, as the removal of interlayer water molecules enables tetrahedral rotation to accommodate the mismatch between octahedral and tetrahedral sheets in platy kaolinite (Sanematsu and Watanabe, 2016). Thus, in the outermost layer of topsoil, kaolinite is the predominant mineral. Interestingly, XRD, SEM, and TEM observations showed that as depth decreases, the crystallinity and lamellar thickness of kaolinite increases. According to a previous study, this is probably ascribable to the substitution of structural Al by Fe (Jige et al., 2018). As shown in the Mössbauer analysis (TABLE S4),

there is relatively extensive substitution of Al by Fe in clay minerals in the incipient weathering period. However, as weathering proceeds, the extent of this substitution decreases, as Fe is released to form Fe (hydr)oxides. Thus, the inhibition of the kaolinite growth is weakened.

Variation in Fe (hydr)oxide minerals

The parent rock of the studied profile is quartz diorite, which contains the rock-forming and Fe-bearing minerals, biotite and hornblende. During the weathering process, their decomposition results in the dissolution of a large amount of Fe into the fluid. As mentioned, the Mössbauer results show that Fe cations can replace structural Al and Si to form Fe-bearing clay minerals, such as illite, kaolinite, and montmorillonite. It is estimated that Fe-bearing clay minerals account for up to 50% of the Fe in soils and sediments (Luan et al., 2015). Moreover, Fe cations precipitate to form (hydr)oxides, which become dominant in the late stage of weathering. Thus, Fe (hydr)oxide minerals are common secondary minerals with broad distributions (Navrotsky et al., 2008). The transformation pathways of Fe (hydr)oxides are complicated, as they depend on several environmental factors, such as temperature, pH, and redox conditions, and result in the formation of various phases (Larese-Casanova et al., 2012; Schwertmann et al., 2004). Through the Mössbauer and TEM analyses, the main Fe (hydr)oxide minerals in the Renju profile are ferrihydrite, goethite, and hematite, with their relative proportions altering with progressive weathering.

In the presence of Si and phosphorus (P), the oxidation of Fe(II) to Fe(III) is

accelerated, and Fe(III) hydrolyzes to form ferrihydrite, which is a short-range-ordered Fe (hydr)oxide (Galvez et al., 1999; Hu et al., 2022). This process is facilitated in the initial weathering stage, as the weathering of rock-forming minerals increases the concentrations of Si and P in the fluid. Moreover, ferrihydrite is a weakly crystalline, metastable mineral, and an important precursor of Fe oxides with higher stability in soil. Goethite and hematite are the most common of such Fe oxides; the latter forms from ferrihydrite via thermal dehydration or dehydroxylation reactions leading to structural transformation, whereas the former forms from ferrihydrite via dissolution–reprecipitation in solution (Schwertmann and Murad, 1983). The weakly acidic (ca. pH 5, Figure 1) semi-weathered layer favors the dissolution of ferrihydrite to Fe(III), followed by the crystallization of goethite (Schwertmann and Murad, 1983). This process can be accelerated by aqueous Fe(II), as high concentrations of Fe(II) are generated through the dissolution of Fe (hydr)oxides in this layer by dissimilating reducing bacteria (Tomaszewski et al., 2016). Microbially derived aqueous Fe(II) catalyzes the transformation of ferrihydrite to goethite by accelerating Fe(II)–Fe(III) electron transfer in the aqueous and solid phases (Catalano et al., 2010). The phase transformation mechanisms include dissolution/reprecipitation, solid-state recrystallization, and particle-mediated growth (Qafoku et al., 2020). Thus, ferrihydrite and goethite are found together in this layer. However, as the depth decreases, the concentration of goethite increases, and thus is negatively correlated with the concentration of ferrihydrite (Figure 5).

In the completely weathered layer and the extensively weathered topsoil, the warm

926 climate and frequent meteoric water cause a more oxidative condition than those in
927 other layers. This favors the formation of hematite (Figure 5). The transformation of
928 ferrihydrite is a two-stage crystallization process, with goethite and hematite being
929 intermediary and dominant products, respectively, at all pHs and temperatures (Das et
930 al., 2011). At RT, the transformation of ferrihydrite into goethite and then into hematite
931 occurs via a topotactic mechanism, i.e., dehydration and/or arrangement of FeO_6
932 octahedral monomers and polymers. That is, a terminal hydroxyl ligand or a water
933 molecule of an FeO_6 octahedron is displaced by a terminal hydroxyl ligand of another
934 FeO_6 octahedron to form a corner-sharing linkage (Li et al., 2020b). Based on this
935 mechanism, the transformation of goethite to hematite along the profile of the deposit
936 is attributable to changes in the hydrological environment. The groundwater system in
937 regolith includes a vadose (unsaturated) zone above the groundwater table and a
938 saturated zone below the groundwater table. The saturated zone (low section) contains
939 abundant goethite (Huang et al., 2021a), whereas the vadose zone (upper section) is
940 exposed to variations in temperature and humidity that cause the dehydration of
941 goethite, and thus this zone is dominated by hematite (Figure 5). Additionally, the
942 transformation of ferrihydrite and goethite into hematite is constrained by Al
943 substitution. According to previous study (Kubicki et al., 2012), Al substitution slows
944 down the transformation to goethite, as the clustered Al atoms impedes the dissolution
945 of Fe^{3+} as a key step in a dissolution-reprecipitation process. Thus, Al doping favors the
946 formation of hematite over goethite in the transformation of Al-ferrihydrite (Pinney and
947 Morgan, 2013). As the extent of weathering increases, especially in topsoil, the

948 dissolution of clay minerals releases abundant Al(III), which are incorporated into Fe
949 (hydr)oxides, thereby promoting the formation of hematite.

950 The XRD and TEM analyses show that ferrihydrite–kaolinite, goethite–
951 kaolinite/halloysite, and hematite-kaolinite/halloysite composites are distributed in the
952 semi-weathered, completely weathered, and topsoil layers, respectively. Owing to the
953 difference between the ZPCs of kaolinite/halloysite (< 4) and those of Fe (hydr)oxides
954 (6–8), the aforementioned types of species display opposite surface charges, resulting
955 in the formation of composites via electrostatic attraction.

956

957 **REE enrichment**

958 In weathering crust, REEs occur in water-soluble, ion-exchangeable, carbonate-
959 binding, humic-acid-binding, Fe–Mn (hydr)oxide-associated, and residual fraction
960 states (Li et al., 2019). Ion-exchangeable REEs adsorbed onto clay minerals are the
961 most common (Figure 11), consistent with other ion-adsorption-type deposits. However
962 bedrock debris, in addition to refractory minerals, contains considerable concentrations
963 of residual REEs, which are barely mined or even mobile. This means that the
964 contributions of other REE states (e.g., Fe–Mn (hydr)oxide-associated and humic-acid-
965 binding fractions) to REE enrichment and transportation are underestimated. Thus, to
966 exclude the effect of residual fractions, the samples collected from the weathering
967 profile were further extracted to obtain fine particles (those <2 μm in size). This
968 significantly decreased the proportion of residual fractions in total REEs (Figure 11),
969 such that they were barely detected in the fine particle fraction. This was because

compared with common secondary minerals (e.g., clay and Fe–Mn (hydr)oxide minerals), refractory REE-bearing minerals (e.g., monazite and xenotime) have much larger particle sizes and were thus separated in the extraction. In the semi-weathered and completely weathered layers, the proportion of ion-exchangeable REEs in the fine particle fraction (i.e., 60%–90%, Figure 11) is even higher than that in the bulk phase (<60%), especially in the locations that are highly enriched in REEs. This verifies the vital role of clay minerals in the enrichment of REEs.

The distribution of clay minerals in the profile of the deposit shows that its primary clay minerals are kaolinite and halloysite (Figure 3). The mechanisms by which these minerals adsorb REEs have been highlighted in numerous recent studies (Borst et al., 2020; Yang et al., 2019; Zhou et al., 2022). Kaolinite and halloysite are the most important members of kaolin-group 1:1 layer minerals, which consist of alternating tetrahedral sheets and octahedral sheets, containing Si^{4+} and Al^{3+}, respectively. The substitution of tetrahedral Si^{4+} by Al^{3+} creates a permanent negative charge within the layers, but occurs infrequently in kaolin-group 1:1 layer minerals, due to the relatively strong bonding between the 1:1 layers (Balan et al., 2014). Thus, the cation-exchange capacity (CEC) of this group of minerals is typically lower than that of 2:1 layer clay minerals. Instead, most charge is pH-dependent and generated from the aluminol (Al-OH) surface of gibbsite basal planes and the hydroxyl groups at edge sites and defects (Liu et al., 2022). Thus, the adsorption capacity of REEs on halloysite and kaolinite is constrained by the pH and ionic strength of weathering fluid. For example, outer-sphere adsorption usually occurs at acidic pHs and low ionic strengths, and results in a full

hydration sphere that is loosely adsorbed to a basal surface via electrostatic attraction (Coppin et al., 2002). With increasing pH and ionic strength, inner-sphere complexes become dominant, such that REEs bond directly with Al-O or Si-O groups on Al-OH or siloxane surfaces, or with the edge sites of clay minerals (Borst et al., 2020). Given the pH variation (4–6) and low ionic strength along the weathering profile, the enrichment of REEs in kaolinite and halloysite occurs mainly through electrostatic attraction to form outer-sphere complexes, which are more leachable than inner-sphere complexes. This accounts for ion-exchangeable REEs (i.e., Nd and Yb) being extensively extracted by $(NH_4)_2SO_4$ in the simulated adsorption experiment. Thus, ion-adsorption-type REEs deposits are currently mined using in-situ leaching technology, wherein leaching agents containing $(NH_4)_2SO_4$ are pumped into ore bodies to recover REE ions through ion exchange reaction (Moldoveanu and Papangelakis, 2013).

In the REE-enriched layer, kaolinite and halloysite are the main clay minerals and are present in similar concentrations. However, their contributions to REE accumulation are not easy to distinguish and remain debated. Theoretically, compared with platy kaolinite, tubular halloysite has a larger surface area and more abundant pores, and thus a higher adsorption capacity (Zhou et al., 2022). However, the adsorption experiment showed that kaolinite has a higher SSA-normalized adsorption capacity than halloysite (Yang et al., 2019). This is probably ascribable to the fact that in halloysite, active sites (i.e., Al-OH) are located on the internal surface of the tubular structure, meaning that steric effects hinder REEs' abilities to contact this internal surface (Yuan et al., 2015). The TEM observations (Figures 6–10) reveal that

morphology, crystallinity, and particle size change with the extent of weathering, which also affect the adsorption abilities of minerals. This makes it hard to clearly differentiate the REE enrichment due to kaolinite and halloysite, respectively, and this requires further investigation.

The Fe–Mn (hydr)oxide-associated fraction of REEs accounts for ca. 20% of REEs at most depths, but over 50% in the topsoil and semi-weathered layer. This indicates the non-negligible contribution of Fe–Mn (hydr)oxides to REE enrichment. However, as the concentration of Fe is 10–100 times that of Mn (Figure 1), REEs in these fractions are likely to be bonded to Fe (hydr)oxides rather than Mn (hydr)oxides. In contrast to the adsorption of REEs onto clay minerals, their adsorption onto Fe (hydr)oxides largely results in the formation inner-sphere complexes, which are not affected by ionic strength (Quinn et al., 2006). Ohta et al. (2009a) used extended X-ray absorption fine structure (EXAFS) spectroscopy to study the local structure of REEs adsorbed onto Fe (hydr)oxides. They found that REE–O bond distances were largely different from those in aqueous REEs, as the Fe atom appeared in the second coordination shell and had a coordination number of two. Most studies have suggested that adsorption geometries include monodentate, bidentate edge-sharing, and bidentate corner-sharing complexes (Stumpf et al., 2006). Thus, compared with REEs adsorbed onto clay minerals as outer-sphere species, those adsorbed onto Fe (hydr)oxides as inner-sphere species have higher stability. This also explains the observation in the present desorption experiment using $(NH_4)_2SO_4$, i.e., ion-exchangeable REEs were easily removed, whereas most of the Fe (hydr)oxide-associated fraction was retained.

Thus, both clay minerals and Fe (hydr)oxides are important hosts for adsorbed REEs, but they adsorb REEs by forming outer-sphere and inner-sphere species, respectively, via different adsorption mechanisms. Thus, the Sips model has the best fit with the REE adsorption isotherms, suggesting that REE adsorption occurs at more than one active site through a combination of physical and chemical adsorption processes. In addition, the clay mineral and Fe (hydr)oxide composites display identical adsorption characteristics for heavy metals, e.g., Pb, Ni, Cd, and Zn (Gomez-Gonzalez et al., 2018; Oliveira et al., 2003), as they do for REEs. The combination of clay minerals with Fe (hydr)oxides significantly increases the SSA and abundance of micropores, resulting in this combination showing an enhanced capacity to adsorb the above-mentioned metals (Zhuang and Yu, 2002).

The chemical composition and TEM/SEM observations show that the concentration of clay minerals is significantly higher than that of Fe (hydr)oxides in the deposit. Therefore, as revealed by the sequential extraction results, the proportion of ion-exchangeable REEs is obviously higher than those of amorphous and crystalline Fe (hydr)oxide-associated REEs. Moreover, compared with crystalline Fe (hydr)oxides, amorphous Fe (hydr)oxides have a larger surface area, and more surface hydroxyl groups generated from lattice defects, and accordingly scavenge more REEs (Koeppenkastrop and Carlo, 1992). Thus, variations in mineral phases and morphologies can explain the distribution characteristics of REEs along the profile of the deposit. The main species of REEs, i.e., ion-exchangeable and Fe (hydr)oxide-associated species, are enriched in the completely weathered layer (i.e., at 16–28 m,

Figures 2 and 11). In this layer, clay minerals are dominated by kaolinite and halloysite, while Fe (hydr)oxides mainly include goethite and hematite. The "booklet" kaolinite and nano-sized semi-unfolded halloysite expose abundant hydroxyl groups at edge sites and octahedral Al-OH, respectively (Yang et al., 2019). However, compared with other layers, both goethite and hematite in this layer have significantly lower particle sizes (100–300 nm and 20–50 nm, respectively), which results in maximal adsorption of REEs. However, with an increase in depth, Fe (hydr)oxide-associated REEs become predominant in the semi-weathered layer, accounting for 50%–90% of the REEs. This is ascribable to the fact that in these layers, Fe (hydr)oxide is mainly ferrihydrite, which has a large SSA and abundant surface hydroxyl groups. This endows ferrihydrite with a higher REE-adsorption capacity than those of other species, leading to the adsorption of more REEs onto (especially amorphous) Fe (hydr)oxides. In the topsoil, the proportion of Fe (hydr)oxide-associated REEs is also comparable to that of ion-exchangeable REEs. This is ascribable to the oxidation of Ce(III) by Fe (hydr)oxides to form cerianite (CeO_2), which is discussed in the following section.

REE fractionation

REE fractionation is controlled by several factors, including aqueous speciation, oxidation–reduction reactions, and variations in the atomic configurations of REEs (Wood, 1990). For instance, owing to the regular variation of physicochemical properties (e.g., variations in ionic radii, which cause LREE–HREE fractionation, and variations in oxidation states, which cause Ce anomalies) across the REE series (Bau,

1999), REEs are assumed to fractionate during migration and accumulation in the weathering crust. This accounts for REEs' different fractionation characteristics across the weathering crust.

Ce anomaly

Ce is the only REE that can be oxidized in the natural environment. Ce(III) is soluble and readily oxidized to Ce(IV) under aerobic conditions, resulting in its precipitation as CeO_2 (cerianite) (Janots et al., 2015). When Ce(III) is adsorbed onto clay minerals, it is preserved in eight- to nine-coordinate outer-sphere-hydrated complexes that do not decouple from other REEs (Borst et al., 2020). Conversely, Ce(III) is adsorbed by Fe–Mn (hydr)oxides through oxidative scavenging (Bau, 1999). Given the redox potential and semiconducting properties of Mn (hydr)oxides, they promote the oxidation of Ce(III) to form electron acceptors (Takahashi et al., 2000), whereas Fe (hydr)oxides catalyze electron transfer between Ce(III) and Mn (hydr)oxides (Bau and Koschinsky, 2009). This indicates that besides Ce oxidation by oxygen to form cerianite, Fe (hydr)oxides rather than clay minerals are significant mediate in Ce oxidation in the weathering profile. Thus, although the weathering crust contains much less Mn than Fe, the effect of Mn (hydr)oxides on Ce(III) oxidation is non-negligible.

Throughout the studied profile (2–55 m), the positive Ce anomaly is preserved in the amorphous and crystalline Fe (hydr)oxide-associated REE fractions, leading to a negative Ce anomaly in the ion-exchangeable REE fraction (Figure S7). Thus, to exclude the effect of the Ce anomaly, the fractionation of LREEs and HREEs was

discriminated by determining (LREE-Ce)/HREE values. Moreover, in the topsoil of an oxic environment, abundant hematite is present; it functions as a semiconducting mineral that facilitates electron transfer from Ce(III) to dissolved O_2 (Hu et al., 2023). Thus, cerianite aggregates usually adhere to nanoscale hematite clusters. This means that most of the Ce atoms released by the chemical weathering of REE-bearing minerals fail to migrate with other REEs, and instead adhere to Fe (hydr)oxide surfaces. Therefore, at depths of 2 and 10 m in the deposit, the proportion of Fe (hydr)oxide-associated REEs is comparable to or surpasses that of the ion-exchangeable REEs (Figure 11). However, in our adsorption experiment, the Ce anomaly was not detected in either the Fe (hydr)oxide-associated or ion-exchangeable fractions, which was probably due to the short reaction time.

LREE–HREE fractionation

As aforementioned, in the weathering crust environment with a weakly acidic pH and low ionic strength, REEs are adsorbed onto clay mineral surfaces through electrostatic attraction, such that REEs exist as outer-sphere species with a full hydration sphere. Borst et al. (2020) reported an eightfold- and nine-fold coordination sphere for REEs associated with kaolinite and halloysite, combined with the absence of a second shell of Al or Si atoms, which is similar to those of fluorcarbonates and REEs in aqueous solution. Thus, the physical adsorption of REEs by clay minerals could not cause extensive fractionation of LREEs and HREEs. This accounts for the nearly flat pattern of ion-exchangeable REEs on reacted Bt-60d, corresponding to an (LREE−

Ce)/HREE value of 1.01. However, this appears to contradict the pattern of ion-exchangeable REEs in the Renju profile. For instance, after normalization against the REE patterns of parent rock, the ion-exchangeable REEs display a right-inclined pattern with (LREE-Ce)/HREE values larger than 1 in the A and upper B horizons, suggesting that these horizons are enriched in LREEs. However, as the depth increases, the pattern changes to left-inclined, with (LREE-Ce)/HREE values decreasing to ca. 0.5 in the lower B and C horizons, indicating that these horizons are enriched in HREEs.

Such spatial distribution differences are probably ascribable to the differences between the mobilities of LREEs and HREEs. Theoretical calculations and aqueous chemistry experiments showed that REEs form strong and predominantly electrostatic complexes with ligands in aqueous fluids, including fluoride and carbonate (bicarbonate), with the stability of these complexes increasing as atomic number increases (i.e., ionic radius decreases) (Wood, 1990). Carbonate (bicarbonate) complexes of REEs are the most important inorganic species involved in the transport of REEs in regolithic groundwater (Liu et al., 2017). HREEs have a stronger ability than LREEs to complex with carbonate (bicarbonate) and are more likely to migrate downward (Ohta and Kawabe, 2000). However, research shows that carbonate contribution can be negligible at low pH (< 5.5) under air-equilibrium condition (Takahashi et al., 1999); thus, REEs probably mobile as bicarbonate complexes and free REE^{3+} in the upper completely weathered layer with low pH and as carbonate complexes in the lower layers with higher pH. Besides, inner sphere complexes of REE with -OH group at clay minerals surface could form above pH 6, which shows a larger

distribution coefficients (K_d) for heavier REEs in REEs adsorption (Takahashi et al., 2004). The above factors lead to the enrichment of LREEs and HREEs in the upper and lower parts of the weathering crust, respectively. Interestingly, when the pattern was normalized by that of whole rock at the same depth to eliminate the effect of complexation by inorganic ligands during downward transfer, the (LREE-Ce)/HREE values at most depths were approximately 1 (1.05–1.15). This further confirms the non-selective adsorption of REEs by clay minerals.

REE adsorption onto Fe (hydr)oxides exhibits a strong dependence on pH and a negligible dependence on ionic strength, suggesting that it involves chemical adsorption via the formation of inner-sphere species. This was verified by an Fe atom being found in the second coordination shell via EXAFS analysis (Ohta et al., 2009a). Across the REE group, effective ionic radii decrease as atomic numbers increase, resulting in variations in adsorption configurations. For example, LREEs form eightfold- and nine-fold coordination spheres, whereas HREEs form only an eightfold coordination sphere. In addition, with increasing atomic number, REE–Fe distances shorten from 3.72 to 3.41 Å (Ohta et al., 2009a; Ohta et al., 2009b). Moreover, HREEs are bound in monodentate or bidentate complexes, whereas LREEs are bound in monodentate complexes.

The adsorption of REEs onto Fe (hydr)oxides can be regarded as the transformation of aqueous hydrated REE cations to dehydrated cations; thus, surface complexation constants can be correlated with the first hydrolysis constants (Wood, 1990), which increase as atomic number increases. This accounts for the greater affinity of HREEs

than LREEs for Fe (hydr)oxides, and thus the depletion of LREEs. Therefore, in fractions in which REEs are associated with crystallized and amorphous Fe (hydr)oxides, both bedrock and whole-rock normalized (LREE-Ce)/HREE ratios are mostly less than 1 along the profile of the deposit. Interestingly, unlike in the ion-exchangeable fraction, the complexation of REEs with carbonate ions in the leachate could not reverse the fractionation of the Fe (hydr)oxide-associated fraction. This is probably ascribable to the enhanced adsorption of $REECO_3^+$ and REEs at low carbonate concentrations. Likewise, on the Bt-60d sample after REE adsorption, both amorphous and crystalline Fe (hydr)oxide-associated REEs showed weakly and markedly right-inclined patterns, with (LREE-Ce)/HREE values of 0.68 and 0.48, respectively. This is also reflected in the TEM–EDS mapping: HREEs (e.g., Yb) are mainly distributed on the surface of Fe (hydr)oxides, most of which could not be desorbed by ion exchange with $(NH_4)_2SO_4$ (Leybourne and Johannesson, 2008). Therefore, both the field observations and adsorption experiments illustrate the prominent contribution of Fe (hydr)oxides to dominating enrichment in HREEs..

Compared with amorphous Fe (hydr)oxides, crystalline Fe (hydr)oxides more selectively adsorb HREEs over LREEs. This is evidenced by the smaller (LREE-Ce)/HREE (0.48) and (LREE-Ce)/$HREE_{s/w}$ values of crystalline Fe (hydr)oxides (0.48 and mostly < 0.5, respectively) than those of amorphous Fe (hydr)oxides in Bt-60 and the fine particle fraction of the Renju profile (0.68 and 0.49–0.82, respectively). This is related to the atomic structure of REEs and the surface properties of Fe (hydr)oxides. The crystallization of amorphous Fe (hydr)oxides involves a change in structure and

decrease in SSA. REEs with larger atomic radii are more readily excluded than those with smaller atomic radii from the structure and surface, resulting in greater retention of HREEs than LREEs on crystalline minerals (Yang et al., 2021). However, the coordination number of HREEs (ca. 8) is less than that of LREEs (ca. 8–9). Compared with amorphous minerals, fewer hydroxyl groups and oxygen vacancies are present on crystalline oxides (Yan et al., 2015). Thus, crystalline Fe (hydr)oxides with low surface densities of hydroxyl groups tend to scavenge HREEs, as fewer hydroxyl groups are required for this process.

CONCLUSIONS AND IMPLICATIONS

The distribution characteristics and enrichment mechanisms of REEs, especially those of HREEs, underpin the ore genesis of ion-adsorption-type REE deposits. In the weathering crust, clay minerals and Fe (hydr)oxides are the main secondary minerals responsible for REE adsorption. To the best of our knowledge, the first time, our study reports the formation and phase composition of clay minerals and Fe (hydr)oxide composites in a typical deposit, and distinguishes the aforementioned species' contributions to the accumulation and fractionation of REEs in this deposit. Most REEs are concentrated in the completely weathered horizon, whereas Ce(III) is oxidized and preserved in the topsoil. As weathering proceeds, the desilication process transforms 2:1-type to 1:1-type clay minerals, whereas Fe (hydr)oxides undergo dehydration. In the completely weathered horizon, kaolinite and halloysite are the dominant clay minerals, and goethite and hematite are the dominant Fe (hydr)oxides, and are the main

adsorbents of REE ions. With further weathering, the crystallinity and particle size of minerals increases, resulting in a decrease in their REE-adsorption capacities. The adsorption isotherms of REEs on the composites are well fitted by the Sips model, implying that monolayer REE adsorption occurs at more than one active site. This indicates that clay minerals and Fe (hydr)oxides are both active components. Clay minerals adsorb REEs through electrostatic attraction to form outer-sphere species, which are easily extracted by $(NH_4)_2SO_4$, a typical lixiviant. These ion-exchangeable REEs are the predominant REEs but do not show fractionation. Conversely, Fe (hydr)oxides scavenge REEs through complexation to form inner-sphere species, most of which could not be desorbed by $(NH_4)_2SO_4$. The proportion of Fe (hydr)oxide-associated REEs is considerable and highly enriched in HREEs along the profile of the deposit and in Ce in the topsoil. Amorphous Fe (hydr)oxides immobilize more REEs than crystalline Fe (hydr)oxides, whereas crystalline Fe (hydr)oxides more selectively adsorb HREEs. This highlights the vital role played by Fe (hydr)oxides in the enrichment of HREEs.

The aforementioned results support the exploration and mining of ion-adsorption-type REE deposits. In particular, although the fractionation features of REEs in the weathering crust are largely inherited from bedrock, this study shows that HREEs are preferentially accumulated onto the surface of Fe (hydr)oxides, especially crystalline Fe (hydr)oxides. Thus, it would be instructive to probe HREE resources by examining Fe (hydr)oxides. For example, when concentrations of total REEs are barely detectable, the establishment of spectral parameters of Fe (hydr)oxides would allow rapid

identification of these species via spectroscopic methods, and thus reveal regions enriched in HREEs. However, current mining technology is based on ion-exchange reactions and thus mainly recovers REEs adsorbed onto clay mineral surfaces, which do not show a preference between LREEs and HREEs. Moreover, although lower concentrations of REEs are present on Fe (hydr)oxide surfaces than on ion-exchangeable surfaces, the REEs on the former are almost all HREEs, which have a higher economic value than LREEs. Furthermore, REE adsorption by Fe (hydr)oxides mainly occurs via surface complexation and thus these REEs cannot be effectively extracted via current mining methods, making it necessary to develop new extraction methods and lixiviants for REEs. For example, a recently devised method that extracts REEs through electrification should be applied (Wang et al., 2022), as it enhances acidification at the cathode and reduces the pH, thus promoting dissolution of Fe (hydr)oxides to release HREEs.

ACKNOWLEDGMENTS

This work was financially supported by the National Key R&D Program of China (Grant No. 2021YFC2901701), National Natural Science Foundation of China (Grant No. 42022012), Youth Innovation Promotion Association CAS (Grant No. 2023369) and Science and Technology Planning Project of Guangdong Province, China (Grant No. 2023B1212060048).

APPENDIX A. SUPPLEMENTARY MATERIAL

Supplementary data associated with this article including major element concentration, mössbauer results, geological map of sampling site, schematic of the weathering profile, chondrite-normalized REE patterns, X-ray diffraction patterns of bulk samples, and characterization of Bt-60d sample can be found in the online version, at XXX.

REFERENCES

Anderson, D.W., Saggar, S., Bettany, J.R., and Stewart, J.W.B. (1981) Particle-size factions snd their use in studies of soil organic-matter: I. The nature and distribution of forms of carbon, nitrogen, and sulfur. Soil Science Society Of America Journal, 45(4), 767-772.

Balan, E., Calas, G., and Bish, D.L. (2014) Kaolin-group minerals: from hydrogen-banded layears to environmental recorders. Elements, 10(3), 183-188.

Banfield, J.F., and Eggleton, R.A. (1990) Analytical transmission electron-microscope studies of plagioclase, muscovite, and K-feldspar weathering. Clays and Clay Minerals, 38(1), 77-89.

Bao, Z.W., and Zhao, Z.H. (2008) Geochemistry of mineralization with exchangeable REY in the weathering crusts of granitic rocks in South China. Ore Geology Reviews, 33(3-4), 519-535.

Bau, M. (1999) Scavenging of dissolved yttrium and rare earths by precipitating iron oxyhydroxide: Experimental evidence for Ce oxidation, Y-Ho fractionation, and lanthanide tetrad effect. Geochimica Et Cosmochimica Acta, 63(1), 67-77.

Bau, M., and Koschinsky, A. (2009) Oxidative scavenging of cerium on hydrous Fe oxide: Evidence from the distribution of rare earth elements and yttrium between Fe oxides and Mn oxides in hydrogenetic ferromanganese crusts. Geochemical Journal, 43(1), 37-47.

Berger, A., Janots, E., Gnos, E., Frei, R., and Bernier, F. (2014) Rare earth element mineralogy and geochemistry in a laterite profile from Madagascar. Applied

Geochemistry, 41, 218-228.

Borst, A.M., Smith, M.P., Finch, A.A., Estrade, G., Villanova-de-Benavent, C., Nason, P., Marquis, E., Horsburgh, N.J., Goodenough, K.M., Xu, C., Kynicky, J., and Geraki, K. (2020) Adsorption of rare earth elements in regolith-hosted clay deposits. Nature Communications, 11(1), 4386.

Catalano, J.G., Fenter, P., Park, C., Zhang, Z., and Rosso, K.M. (2010) Structure and oxidation state of hematite surfaces reacted with aqueous Fe(II) at acidic and neutral pH. Geochimica Et Cosmochimica Acta, 74(5), 1498-1512.

Chakhmouradian, A.R., and Wall, F. (2012) Rare earth elements: minerals, mines, magnets (and more). Elements, 8(5), 333-340.

Chen, C.M., Barcellos, D., Richter, D.D., Schroeder, P.A., and Thompson, A. (2019) Redoximorphic Bt horizons of the Calhoun CZO soils exhibit depth-dependent iron-oxide crystallinity. Journal of Soils and Sediments, 19(2), 785-797.

Churchman, G.J., Whitton, J.S., Claridge, G.G.C., and Theng, B.K.G. (1984) Intercalation method using formamide for differentiating halloysite form kaolinite. Clays and Clay Minerals, 32(4), 241-248.

Coppin, F., Berger, G., Bauer, A., Castet, S., and Loubet, M. (2002) Sorption of lanthanides on smectite and kaolinite. Chemical Geology, 182(1), 57-68.

Cornell, R.M., and Schwertmann, U. (1996) The iron oxide: Structure, Properties, Reactions, Occurences and Uses. Wiley-VCH Verlag GmbH & Co. KGaA, Weinheim.

Costa, N.O., Botelho, N.F., and Garnier, J. (2020) Concentration of rare earth elements

in the Faixa Placha tin deposit, Pedra Branca A-Type Granitic Massif, central Brazil, and its potential for ion-adsorption-type REE-Y mineralization. Ore Geology Reviews, 123, 103606.

Das, S., Hendry, M.J., and Essilfie-Dughan, J. (2011) Transformation of two-line ferrihydrite to goethite and hematite as a function of pH and temperature. Environmental Science & Technology, 45(1), 268-275.

Dill, H. G. (2016) Kaolin: Soil, rock and ore: From the mineral to the magmatic, sedimentary and metamorphic environments. Earth-Science Reviews, 16-129.

Galán, E., and Ferrell, R.E. (2013) Chapter 3 - Genesis of Clay Minerals. In F. Bergaya, and G. Lagaly, Eds. Developments in Clay Science, 5. Elsevier, Amsterdam.

Galvez, N., Barron, V., and Torrent, J. (1999) Effect of phosphate on the crystallization of hematite, goethite, and lepidocrocite from ferrihydrite. Clays and Clay Minerals, 47(3), 304-311.

Gomez-Gonzalez, M.A., Villalobos, M., Marco, J.F., Garcia-Guinea, J., Bolea, E., Laborda, F., and Garrido, F. (2018) Iron oxide-clay composite vectors on long-distance transport of arsenic and toxic metals in mining-affected areas. Chemosphere, 197, 759-767.

Hu, E.R., Liu, M.C., Wang, F., Lv, B.S., and Wu, J. (2022) Effects of phosphate, silicate, humic acid, and calcium on the release of As(V) co-precipitated with Fe(III) and Fe(II) during aging. Journal of Hazardous Materials, 438, 129478.

Hu, S.W., Zheng, L.R., Zhang, H.Y., Chen, G.J., Yang, Y., Ouyang, Z.Z., Chen, S.L., Gao, K., Liu, C.X., Wang, Q., and Liu, T.X. (2023) Hematite-mediated Mn(II)

abiotic oxidation under oxic conditions: pH effect and mineralization. Journal of Colloid and Interface Science, 636, 267-278.

Huang, J., He, H.P., Tan, W., Liang, X.L., Ma, L.Y., Wang, Y.Y., Qin, X.R., and Zhu, J.X. (2021a) Groundwater controls REE mineralisation in the regolith of South China. Chemical Geology, 577, 120295.

Huang, J., Tan, W., Liang, X.L., He, H.P., Ma, L.Y., Bao, Z.W., and Zhu, J.X. (2021b) REE fractionation controlled by REE speciation during formation of the Renju regolith-hosted REE deposits in Guangdong Province, South China. Ore Geology Reviews, 134.

Inoue, A., Utada, M., and Hatta, T. (2012) Halloysite-to-kaolinite transformation by dissolution and recrystallization during weathering of crystalline rocks. Clay Minerals, 47(3), 373-390.

Janots, E., Bernier, F., Brunet, F., Muñoz, M., Trcera, N., Berger, A., and Lanson, M. (2015) Ce(III) and Ce(IV) (re)distribution and fractionation in a laterite profile from Madagascar: Insights from in situ XANES spectroscopy at the Ce L_{III}-edge. Geochimica Et Cosmochimica Acta, 153, 134-148.

Jeong, G.Y. (1998) Formation of vermicular kaolinite from halloysite aggregates in the weathering of plagioclase. Clays and Clay Minerals, 46(3), 270-279.

Jige, M., Takagi, T., Takahashi, Y., Kurisu, M., Tsunazawa, Y., Morimoto, K., Hoshino, M., and Tsukimura, K. (2018) Fe-kaolinite in granite saprolite beneath sedimentary kaolin deposits: A mode of Fe substitution for Al in kaolinite. American Mineralogist, 103(7), 1126-1135.

Kasay, G.M., Bolarinwa, A.T., Aromolaran, O.K., Nzolang, C., and Kivava, A.S. (2022) Rare Earth Element Deposits and Their Prospects in the Democratic Republic of Congo. Mining Metallurgy & Exploration, 39(2), 625-642.

Koeppenkastrop, D., and Carlo, E.H.D. (1992) Sorption of rare-earth elements from seawater onto synthetic mineral particles: An experimental approach. Chemical Geology, 95(3-4), 251-263.

Kubicki, J.D., Aryanpour, M., Kabalan, L., and Zhu, Q. (2012) Quantum mechanical calculations on Fe-O-H nanoparticles. Geoderma, 189, 236-242.

Larese-Casanova, P., Kappler, A., and Haderlein, S.B. (2012) Heterogeneous oxidation of Fe(II) on iron oxides in aqueous systems: Identification and controls of Fe(III) product formation. Geochimica Et Cosmochimica Acta, 91, 171-186.

Leybourne, M.I., and Johannesson, K.H. (2008) Rare earth elements (REE) and yttrium in stream waters, stream sediments, and Fe-Mn oxyhydroxides: Fractionation, speciation, and controls over REE plus Y patterns in the surface environment. Geochimica Et Cosmochimica Acta, 72(24), 5962-5983.

Li, M.Y.H., Kwong, H.T., Williams-Jones, A.E., and Zhou, M.F. (2021) The thermodynamics of rare earth element liberation, mobilization and supergene enrichment during groundwater-regolith interaction. Geochimica et Cosmochimica Acta, 330, 258-277.

Li, M.Y.H., Zhao, W.W., and Zhou, M.F. (2017) Nature of parent rocks, mineralization styles and ore genesis of regolithhosted REE deposits in South China: An integrated genetic model. Journal Of Asian Earth Sciences, 148, 65-95.

1372 Li, M.Y.H., and Zhou, M.F. (2020) The role of clay minerals in formation of the
1373 regolith-hosted heavy rare earth element deposits. American Mineralogist, 105(1),
1374 92-108.
1375 Li, M.Y.H., Zhou, M.F., and Williams-Jones, A.E. (2019) The genesis of regolith-hosted
1376 heavy rare earth element deposits: Insights from the world-class Zudong deposit in
1377 Jiangxi province, South China. Economic Geology, 114(3), 541-568.
1378 Li, S.Y., He, H.P., Tao, Q., Zhu, J.X., Tan, W., Ji, S.C., Yang, Y.P., and Zhang, C.Q.
1379 (2020a) Kaolinization of 2:1 type clay minerals with different swelling properties.
1380 American Mineralogist, 105(5), 687-696.
1381 Li, X.R., Liang, X.L., He, H.P., Li, J.T., Ma, L.Y., Tan, W., Zhong, Y., Zhu, J.X., Zhou,
1382 M.F., and Dong, H.L. (2022) Microorganisms Accelerate REE Mineralization in
1383 Supergene Environments. Applied and Environmental Microbiology, 88(13), 1-18.
1384 Li, Y., Yang, M.J., Pentrak, M., He, H.P., and Arai, Y. (2020b) Carbonate-enhanced
1385 transformation of ferrihydrite to hematite. Environmental Science & Technology,
1386 54(21), 13701-13708.
1387 Liu, H.Y., Pourret, O., Guo, H.M., and Bonhoure, J. (2017) Rare earth elements sorption
1388 to iron oxyhydroxide: Model development and application to groundwater. Applied
1389 Geochemistry, 158-166.
1390 Liu, X.D., Tournassat, C., Grangeon, S., Kalinichev, A.G., Takahashi, Y., and Fernandes,
1391 M.M. (2022) Molecular-level understanding of metal ion retention in clay-rich
1392 materials. Nature Reviews Earth & Environment, 3(7), 461-476.
1393 Luan, F.B., Liu, Y., Griffin, A.M., Gorski, C.A., and Burgos, W.D. (2015) Iron(III)-

bearing clay minerals enhance bioreduction of nitrobenzene by Shewanella putrefaciens CN32. Environmental Science & Technology, 49(3), 1418-1426.

Luo, Y.R., and Byrne, R.H. (2004) Carbonate complexation of yttrium and the rare earth elements in natural waters. Geochimica Et Cosmochimica Acta, 68(4), 691-699.

Ma, J.L., Wei, G.J., Xu, Y.G., Long, W.G., and Sun, W.D. (2007) Mobilization and re-distribution of major and trace elements during extreme weathering of basalt in Hainan Island, South China. Geochimica Et Cosmochimica Acta, 71(13), 3223-3237.

Moldoveanu, G.A., and Papangelakis, V.G. (2013) Recovery of rare earth elements adsorbed on clay minerals: II. Leaching with ammonium sulfate. Hydrometallurgy, 131, 158-166.

Murakami, H., and Ishihara, S. (2008) REE mineralization of weathered crust and clay sediment on granitic rocks in the Sanyo Belt, SW Japan and the southern Jiangxi Province, China. Resource Geology, 58(4), 373-401.

Navrotsky, A., Mazeina, L., and Majzlan, J. (2008) Size-driven structural and thermodynamic complexity in iron oxides. Science, 319(5870), 1635-1638.

Ohta, A., Kagi, H., Nomura, M., Tsuno, H., and Kawabe, I. (2009a) Coordination study of rare earth elements on Fe oxyhydroxide and Mn dioxides: Part I. Influence of a multi-electron excitation on EXAFS analyses of La, Pr, Nd, and Sm. American Mineralogist, 94(4), 467-475.

-. (2009b) Coordination study of rare earth elements on Fe oxyhydroxide and Mn dioxides: Part II. Correspondence of structural change to irregular variations of

partitioning coefficients and tetrad effect variations appearing in interatomic distances. American Mineralogist, 94(4), 476-486.

Ohta, A., and Kawabe, I. (2000) Rare earth element partitioning between Fe oxyhydroxide precipitates and aqueous NaCl solutions doped with $NaHCO_3$: Determinations of rare earth element complexation constants with carbonate ions. Geochemical Journal, 34(6), 439-454.

Oliveira, L.C.A., Rios, R.V.R.A., Fabris, J.D., Sapag, K., Garg, V.K., and Lago, R.M. (2003) Clay-iron oxide magnetic composites for the adsorption of contaminants in water. Applied Clay Science, 22(4), 169-177.

Papoulis, D., Tsolis-Katagas, P., and Katagas, C. (2004) Progressive stages in the formation of kaolin minerals of different morphologies in the weathering of plagioclase. Clays and Clay Minerals, 52(3), 275-286.

Pinney, N., and Morgan, D. (2013) Thermodynamics of Al-substitution in Fe-oxyhydroxides. Geochimica Et Cosmochimica Acta, 120, 514-530.

Qafoku, O., Kovarik, L., Bowden, M.E., Nakouzi, E., Sheng, A.X., Liu, J., Pearce, C.I., and Rosso, K.M. (2020) Nanoscale observations of Fe(II)-induced ferrihydrite transformation. Environmental Science-Nano, 7(10), 2953-2967.

Quinn, K.A., Byrne, R.H., and Schijf, J. (2006) Sorption of yttrium and rare earth elements by amorphous ferric hydroxide: Influence of solution complexation with carbonate. Geochimica Et Cosmochimica Acta, 70(16), 4151-4165.

Ram, R., Becker, M., Brugger, J., Etschmann, B., Burcher-Jones, C., Howard, D., Kooyman, P.J., and Petersen, J. (2019) Characterisation of a rare earth element-

and zirconium-bearing ion-adsorption clay deposit in Madagascar. Chemical Geology, 522, 93-107.

Robic, M., Ristic, M., Krehula, S., and Music, S. (2022) Forced hydrolysis of $FeCl_3$ solutions in the presence of guanylurea phosphate. Colloids and Surfaces a-Physicochemical and Engineering Aspects, 634.

Sakurai, K., Teshima, A., and Kyuma, K. (1990) Changes in zero point of charge (ZPC), specific surface area (SSA), and cation exchange capacity (CEC) of kaolinite and montmorillonite, and strongly weathered soils caused by Fe and Al coatings. Soil Science And Plant Nutrition, 36(1), 73-81.

Sanematsu, K., Kon, Y., Imai, A., Watanabe, K., and Watanabe, Y. (2013) Geochemical and mineralogical characteristics of ion-adsorption type REE mineralization in Phuket, Thailand. Mineralium Deposita, 48(4), 437-451.

Sanematsu, K., and Watanabe, Y. (2016) Characteristics and genesis of ion adsorption-type rare earth element deposits Reviews in Economic Geology, 18, 55-79.

Schwertmann, U., Friedl, J., Stanjek, H., and Schulze, D.G. (2000) The effect of Al on Fe oxides. XIX. Formation of Al-substituted hematite from ferrihydrite at 25 °C and pH 4 to 7. Clays and Clay Minerals, 48(2), 159-172.

Schwertmann, U., and Murad, E. (1983) Effect of pH on the formation of goethite and hematite from ferrihydrite. Clays and Clay Minerals, 31(4), 277-284.

Schwertmann, U., Stanjek, H., and Becher, H.H. (2004) Long-term in vitro transformation of 2-line ferrihydrite to goethite/hematite at 4, 10, 15 and 25 °C. Clay Minerals, 39(4), 433-438.

Singh, B., and Gilkes, R.J. (1991) Weathering of a chromian muscovite to kaolinite. Clays and Clay Minerals, 39(6), 571-579.

Stumpf, S., Stumpf, T., Dardenne, K., Hennig, C., Foerstendorf, H., Klenze, R., and Fanghanel, T. (2006) Sorption of Am(III) onto 6-line- ferrihydrite and its alteration products: Investigations by EXAFS. Environmental Science & Technology, 40(11), 3522-3528.

Takahashi, Y., Minai, Y., Ambe, S., Makide, Y., and Ambe, F. (1999) Comparison of adsorption behavior of multiple inorganic ions on kaolinite and silica in the presence of humic acid using the multitracer technique. Geochimica Et Cosmochimica Acta, 63(6), 815-836.

Takahashi, Y., Shimizu, H., Usui, A., Kagi, H., and Nomura, M. (2000) Direct observation of tetravalent cerium in ferromanganese nodules and crusts by X-ray-absorption near-edge structure (XANES). Geochimica et Cosmochimica Acta, 64(17), 2929-2935.

Takahashi, Y., Tada, A., and Shimizu, H. (2004) Distribution pattern of rare earth ions between water and montmorillonite and its relation to the sorbed species of the ions. Analytical Sciences, 20(9), 1301-1306.

Tang, J.W., and Johannesson, K.H. (2010) Ligand extraction of rare earth elements from aquifer sediments: Implications for rare earth element complexation with organic matter in natural waters. Geochimica Et Cosmochimica Acta, 74(23), 6690-6705.

Tomaszewski, E.J., Cronk, S.S., Gorski, C.A., and Ginder-Vogel, M. (2016) The role of dissolved Fe(II) concentration in the mineralogical evolution of Fe (hydr)oxides

during redox cycling. Chemical Geology, 438, 163-170.

Van Ranst, E., Mees, F., De Grave, E., Ye, L., Cornelis, J.T., and Delvaux, B. (2019) Impact of andosolization on pedogenic Fe oxides in ferrallitic soils. Geoderma, 347, 244-251.

Wang, G.F., Xu, J., Ran, L.Y., Zhu, R.L., Ling, B.W., Liang, X.L., Kang, S.C., Wang, Y.Y., Wei, J.M., and Ma, L.Y. (2022) A green and efficient technology to recover rare earth elements from weathering crusts. Nature Sustainability, 6, 81-+.

Wang, J.L., and Guo, X. (2020) Adsorption isotherm models: Classification, physical meaning, application and solving method. Chemosphere, 258, 127279.

White, A.F., Bullen, T.D., Schulz, M.S., Blum, A.E., Huntington, T.G., and Peters, N.E. (2001) Differential rates of feldspar weathering in granitic regoliths. Geochimica Et Cosmochimica Acta, 65(6), 847-869.

Wilson, M.J. (2004) Weathering of the primary rock-forming minerals: processes, products and rates. Clay Minerals, 39(3), 233-266.

Wood, S.A. (1990) The aqueous geochemistry of the rare-earth elements and yttrium .1. Review of available low-temperature data for inorganic complexes and the inorganic REE speciation of natural-waters. Chemical Geology, 82(1-2), 159-186.

Xu, C., Kynicky, J., Smith, M.P., Kopriva, A., Brtnicky, M., Urubek, T., Yang, Y.H., Zhao, Z., He, C., and Song, W.L. (2017) Origin of heavy rare earth mineralization in South China. Nature Communications, 8, 14598.

Yan, X.D., Tian, L.H., He, M., and Chen, X.B. (2015) Three-dimensional crystalline/amorphous Co/Co_3O_4 core/shell nanosheets as efficient electrocatalysts

for the hydrogen evolution reaction. Nano Letters, 15(9), 6015-6021.

Yang, M.J., Liang, X.L., Li, Y., He, H.P., Zhu, R.L., and Arai, Y. (2021) Ferrihydrite transformation impacted by adsorption and structural incorporation of rare earth elements. ACS Earth and Space Chemistry, 5(10), 2768-2777.

Yang, M.J., Liang, X.L., Ma, L.Y., Huang, J., He, H.P., and Zhu, J.X. (2019) Adsorption of REEs on kaolinite and halloysite: A link to the REE distribution on clays in the weathering crust of granite. Chemical Geology, 525, 210-217.

Yaraghi, A., Ariffin, K.S., and Baharun, N. (2020) Comparison of characteristics and geochemical behaviors of REEs in two weathered granitic profiles generated from metamictized bedrocks in Western Peninsular Malaysia. Journal of Asian Earth Sciences, 199, 104385.

Yuan, P., Tan, D.Y., and Annabi-Bergaya, F. (2015) Properties and applications of halloysite nanotubes: recent research advances and future prospects. Applied Clay Science, 112, 75-93.

Yuan, P., Tan, D.Y., Annabi-Bergaya, F., Yan, W.C., Fan, M.D., Liu, D., and He, H.P. (2012) Changes in structure, morphology, porosity, and surface activity of mesoporous halloysite nanotubes under heating. Clays and Clay Minerals, 60(6), 561-573.

Zhou, J.M., Liu, H.M., Liu, D., Yuan, P., Bu, H.L., Du, P.X., Fan, W.X., and Li, M.Y. (2022) Sorption/desorption of Eu(III) on halloysite and kaolinite. Applied Clay Science, 216, 106356.

Zhuang, J., and Yu, G.R. (2002) Effects of surface coatings on electrochemical

properties and contaminant sorption of clay minerals. Chemosphere, 49(6), 619-628.

FIGURE CAPTIONS

Figure 1. Variation in chemical alteration index (CIA, a), soil pH (b), total rare earth element (REE) concentration (c) and major element concentrations (e, f, g, and h) and ratio of light REEs to heavy REEs (d) with depth in the weathering profile of the Renju deposit.

Figure 2. Variations in the proportions of fractions of different particle sizes with depth (a) and the distributions of rare earth elements in the fine particle fraction and bulk samples at various depths (b).

Figure 3. X-ray diffraction patterns (a) and mineral compositions (b) of the fine particle fractions in different soil horizons. Abbreviations: Kln = kaolinite; Hal = halloysite; Qtz = quartz; Or = orthoclase; Ilt = illite; Ms = muscovite; Pl = plagioclase; and Mnt = montmorillonite.

Figure 4. X-ray diffraction patterns of the fine particle fractions (< 2 μm) from the A (a), B (b) and C (c) horizons subjected to different treatments, i.e., air-dried oriented samples (black line), formamide-intercalated samples (red line), and ethylene glycol-intercalated samples (blue line). Abbreviations: Kln: kaolinite; Hal: halloysite; Ilt: illite; Ms: muscovite.

Figure 5. Composition of iron species along the weathering profile.

Figure 6. Scanning electron microscopy images of clay minerals and iron (hydr)oxide particles in fine particle fractions collected from topsoil (a), the upper completely weathered layer (b), the lower completely weathered layer (c), and the semi-weathered layer (d). Abbreviations: Kln = kaolinite; Hly = halloysite; and Ms = muscovite.

Figure 7. Transmission electron microscopy (TEM) images, scanning transmission electron microscopy (STEM) images, and corresponding selected-area electron diffraction (SAED) patterns and energy-dispersive X-ray spectroscopy (EDS) spectra of minerals in the semi-weathered layer. a: TEM image and SAED pattern (lower left inserts) of kaolinite and its EDS spectrum (lower right insets); b: TEM image and SAED pattern (lower left insets) of muscovite and its EDS spectrum (upper right insets); c: STEM image of ferrihydrite–clay mineral composite and its fast Fourier transform (FFT) pattern (lower left insets); d: high-resolution TEM of goethite and its FFT pattern (lower left insets). Abbreviations: Kln = kaolinite; Ms = muscovite; Gth = goethite; and Fh = ferrihydrite.

Figure 8. Transmission electron microscopy (TEM) images, scanning transmission electron microscopy (STEM) images, and corresponding selected-area diffraction (SAED) patterns and energy-dispersive X-ray spectroscopy (EDS) spectra of minerals in the lower completely weathered layer. A: TEM image of kaolinite and its EDS spectrum (upper right insets); b: TEM image of illite, with d-spacings of 10 Å, and its EDS spectrum (lower left insets); c: STEM and SAED images of ferrihydrite; d: high-resolution TEM image and fast Fourier transform patterns of goethite (upper right insets) and ferrihydrite (lower left insets). Abbreviations: Kln = kaolinite; Ilt = illite; Gth = goethite; and Fh = ferrihydrite.

Figure 9. Transmission electron microscopy (TEM) images and scanning transmission electron microscopy images of clay minerals and iron (hydr)oxide minerals in the upper completely weathered layer. a: TEM image and selected-area electron diffraction

pattern (lower left insets) of kaolinite and its energy-dispersive X-ray spectroscopy spectrum (upper right insets); b: TEM image of tubular halloysite; c: high-resolution TEM (HRTEM) image (lower left insets) of hematite and its fast Fourier transform (FFT) pattern; d: HRTEM image of goethite and its FFT pattern (lower left insets). Abbreviations: Kln = kaolinite; Hly = halloysite; Hem = hematite; and Gth = goethite.

Figure 10. High-resolution transmission electron microscopy (HRTEM) and scanning transmission electron microscopy (STEM) images of clay minerals and iron (hydr)oxide minerals in the A horizon. a: TEM image with corresponding selected-area electron diffraction pattern (lower left insets) and energy-dispersive X-ray spectroscopy spectrum (upper left insets) of kaolinite; b: STEM image of hematite–kaolinite compound; c, d: HRTEM image of hematite and its fast Fourier transform pattern (inset) (abbreviations: Kln = kaolinite; Hem = hematite).

Figure 11. Proportions of ion-exchangeable rare earth element (REE) (orange bar), organic-associated REE-bearing mineral state (blue bar), amorphous iron–manganese (Fe–Mn) (hydr)oxide associated REE-bearing mineral state (green bar), crystalline Fe–Mn (hydr)oxide-associated REE-bearing mineral state (yellow bar), and residual REE-bearing mineral state (gray bar) in fine particle fractions at different depths.

Figure 12. Variation in parent-rock normalized light rare-earth elements with cerium anomaly/heavy rare-earth elements in specific state/parent rock indicated as (LREE-Ce)/$HREE_{s/p}$ (a) and whole-rock normalized cerium anomaly/heavy rare-earth elements in specific state/whole rock, (LREE-Ce)/$HREE_{s/w}$ (b) with depth in ion-exchangeable and iron (hydr)oxide-associated states.

Figure 13. (a) Plot of logarithm of absorption coefficient (K_d) as a function of atomic number for rare-earth elements (REEs) adsorbed onto Bt-60d. Inset: Adsorption isotherms of Bt-60d for neodymium (black) and ytterbium (red) fitted by the Langmuir adsorption model. (b) Distribution of REEs in ion-exchangeable (black), amorphous (red), and crystallized (blue) iron (hydr)oxide-associated states on Bt-60d. q is the REE concentration in each state, as determined by sequential extraction. q_e is the concentration of adsorbed REEs.

Figure 14. Transmission electron microscopy image of clay mineral–iron(hydr)oxide composite and energy-dispersive X-ray spectroscopy mapping of iron (Fe), aluminum (Al), and neodymium (Nd) on Bt-60d after neodymium (Nd) adsorption (a–f), followed by the extraction of ion-exchangeable Nd (g–i). Adsorption experiment conditions: Bt-60d dosage = 0.5 g L^{-1}; initial concentration of Nd = 10 mg L^{-1}; pH = 6.

Figure 15. Transmission electron microscopy image of clay mineral–iron (hydr)oxide composite and energy-dispersive X-ray spectroscopy mapping of iron (Fe), aluminum (Al), and ytterbium (Yb) on Bt-60d after Yb adsorption (a–f), followed by extraction of ion-exchangeable Yb (g–i). Adsorption experiment conditions: Bt-60d dosage = 0.5 g L^{-1}; initial concentration of Yb = 10 mg L^{-1}; pH = 6.

This is the peer-reviewed, final accepted version for American Mineralogist, published by the Mineralogical Society of America.
The published version is subject to change. Cite as Authors (Year) Title. American Mineralogist, in press.
DOI: https://doi.org/10.2138/am-2023-9217. http://www.minsocam.org/

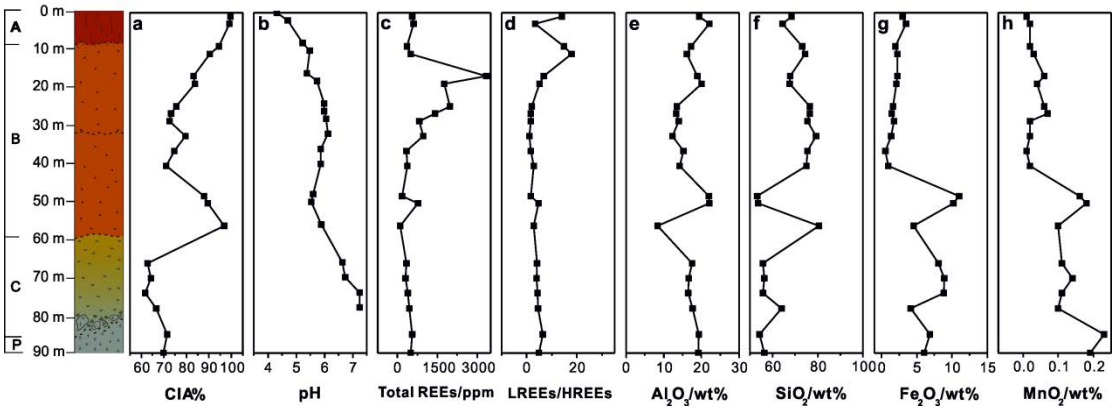

Figure 1

This is the peer-reviewed, final accepted version for American Mineralogist, published by the Mineralogical Society of America.
The published version is subject to change. Cite as Authors (Year) Title. American Mineralogist, in press.
DOI: https://doi.org/10.2138/am-2023-9217. http://www.minsocam.org/

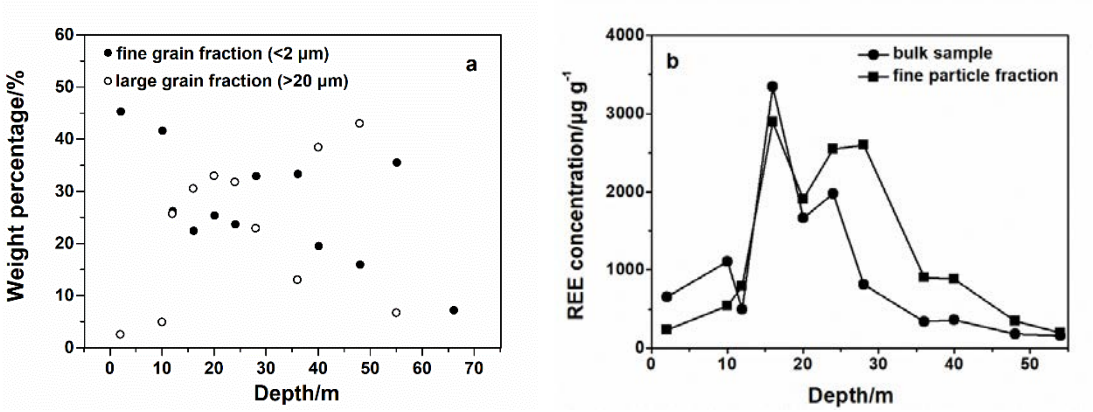

1616 **Figure 2**

1617

This is the peer-reviewed, final accepted version for American Mineralogist, published by the Mineralogical Society of America.
The published version is subject to change. Cite as Authors (Year) Title. American Mineralogist, in press.
DOI: https://doi.org/10.2138/am-2023-9217. http://www.minsocam.org/

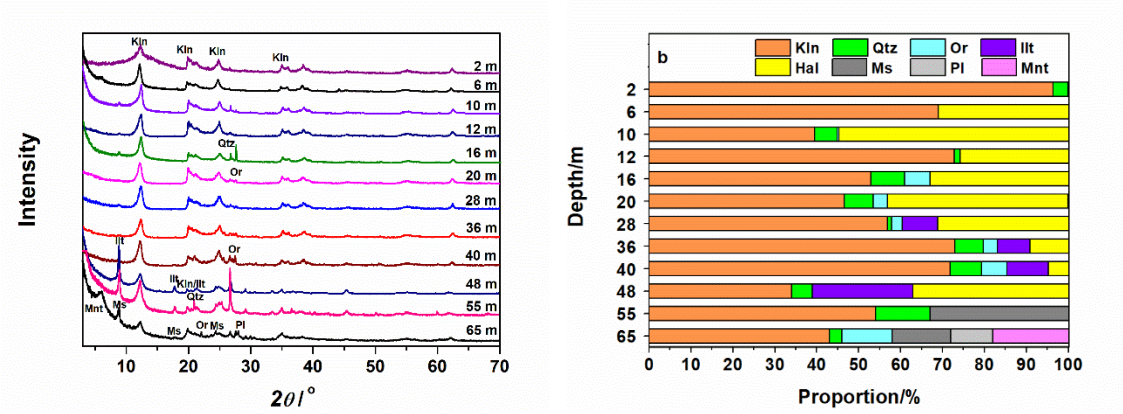

1618 **Figure 3**

1619

This is the peer-reviewed, final accepted version for American Mineralogist, published by the Mineralogical Society of America.
The published version is subject to change. Cite as Authors (Year) Title. American Mineralogist, in press.
DOI: https://doi.org/10.2138/am-2023-9217. http://www.minsocam.org/

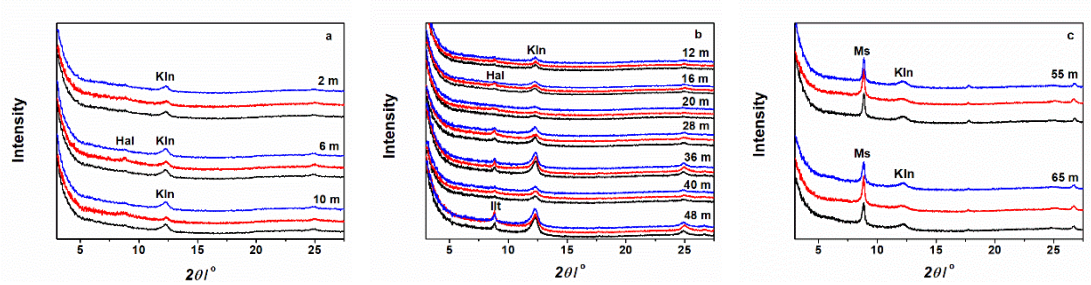

Figure 4

This is the peer-reviewed, final accepted version for American Mineralogist, published by the Mineralogical Society of America.
The published version is subject to change. Cite as Authors (Year) Title. American Mineralogist, in press.
DOI: https://doi.org/10.2138/am-2023-9217. http://www.minsocam.org/

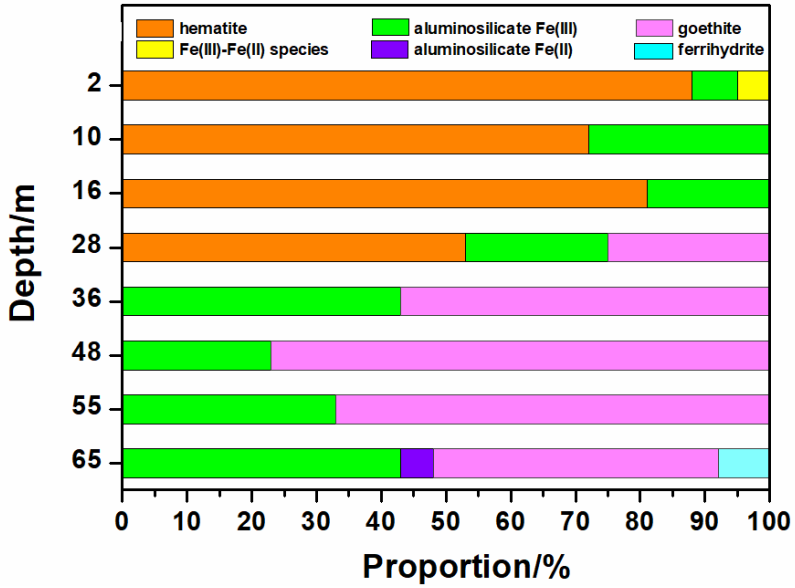

1622

1623 **Figure 5**

1624

This is the peer-reviewed, final accepted version for American Mineralogist, published by the Mineralogical Society of America.
The published version is subject to change. Cite as Authors (Year) Title. American Mineralogist, in press.
DOI: https://doi.org/10.2138/am-2023-9217. http://www.minsocam.org/

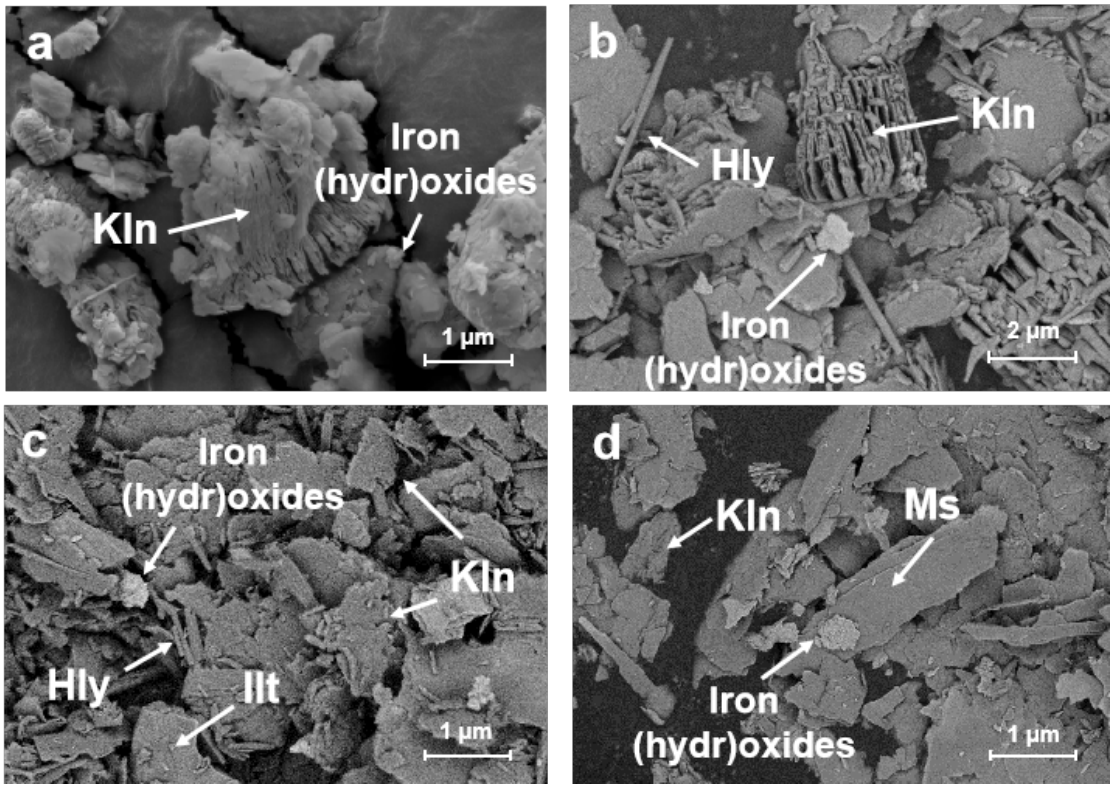

Figure 6

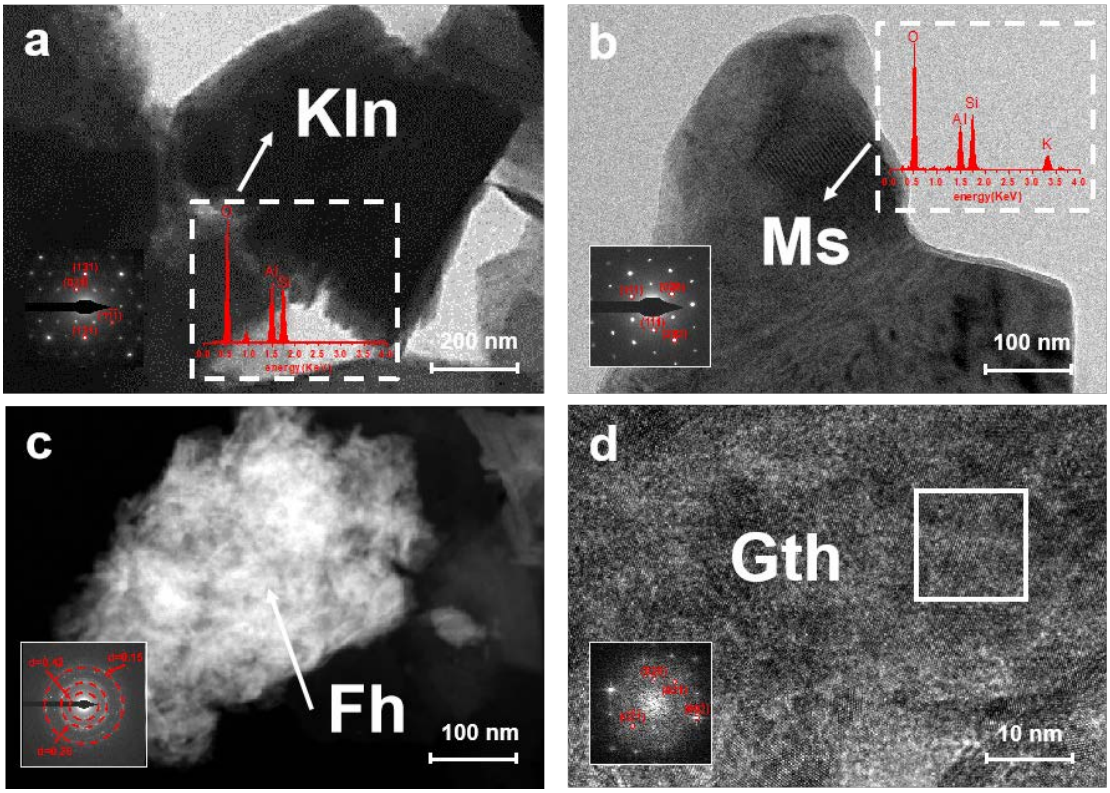

Figure 7

This is the peer-reviewed, final accepted version for American Mineralogist, published by the Mineralogical Society of America.
The published version is subject to change. Cite as Authors (Year) Title. American Mineralogist, in press.
DOI: https://doi.org/10.2138/am-2023-9217. http://www.minsocam.org/

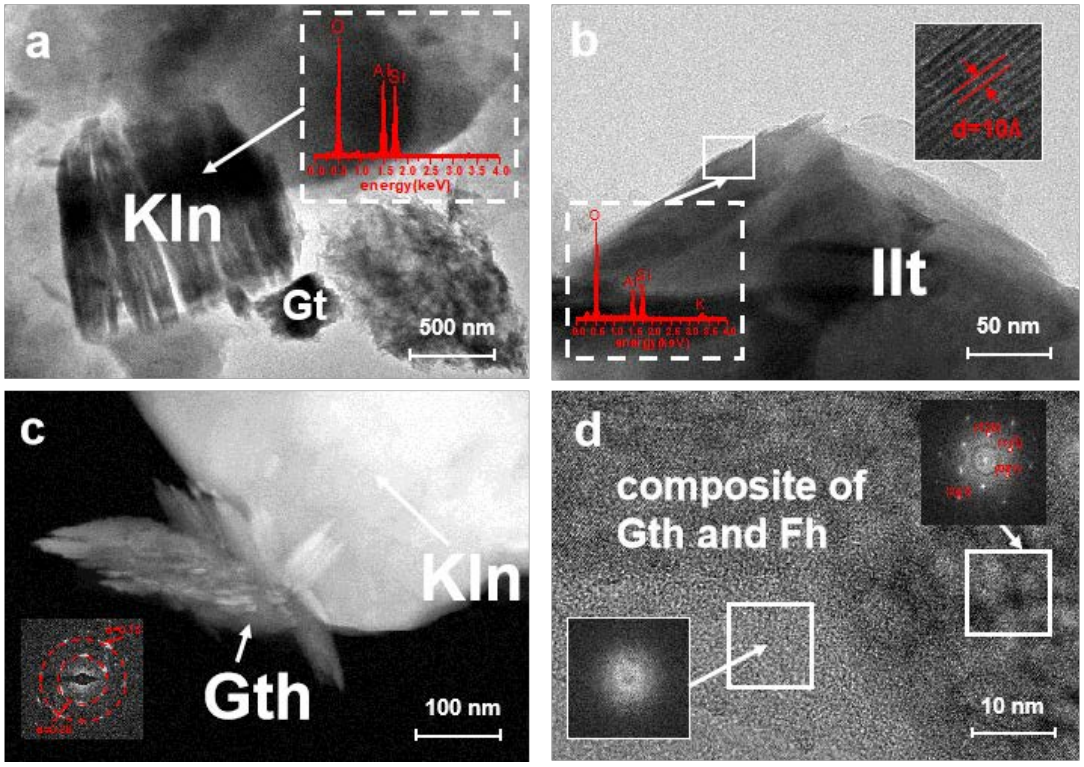

Figure 8

This is the peer-reviewed, final accepted version for American Mineralogist, published by the Mineralogical Society of America.
The published version is subject to change. Cite as Authors (Year) Title. American Mineralogist, in press.
DOI: https://doi.org/10.2138/am-2023-9217. http://www.minsocam.org/

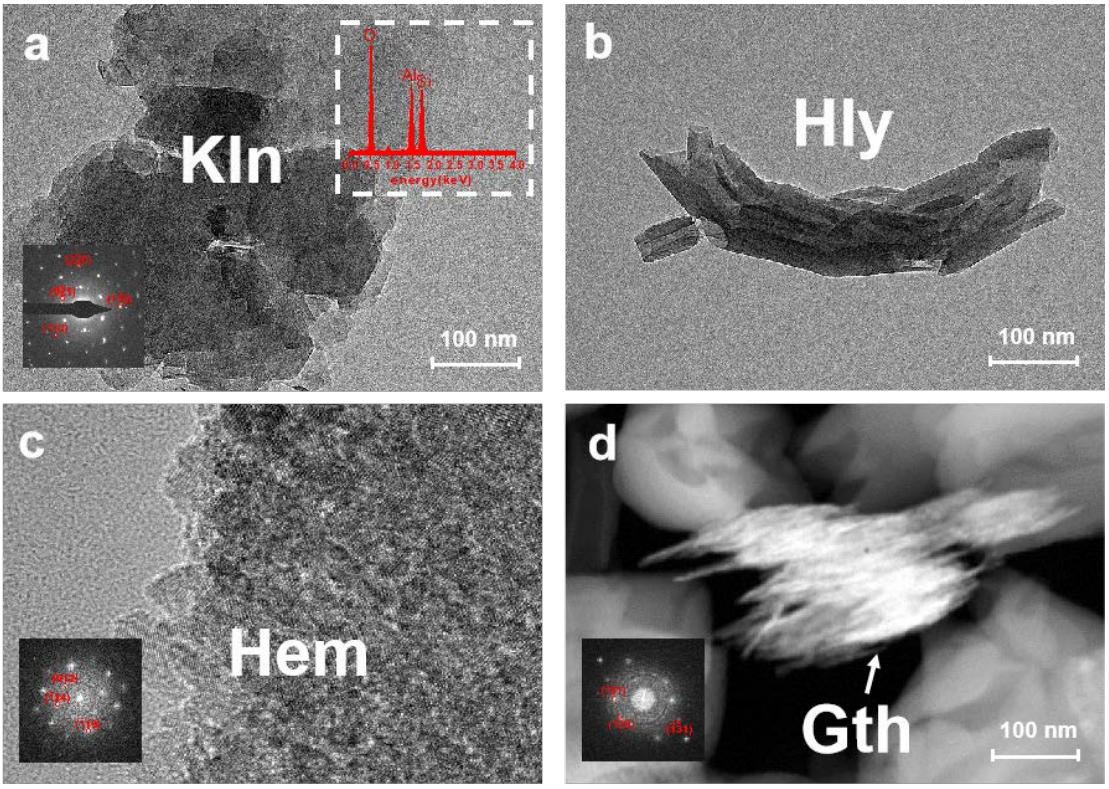

Figure 9

This is the peer-reviewed, final accepted version for American Mineralogist, published by the Mineralogical Society of America.
The published version is subject to change. Cite as Authors (Year) Title. American Mineralogist, in press.
DOI: https://doi.org/10.2138/am-2023-9217. http://www.minsocam.org/

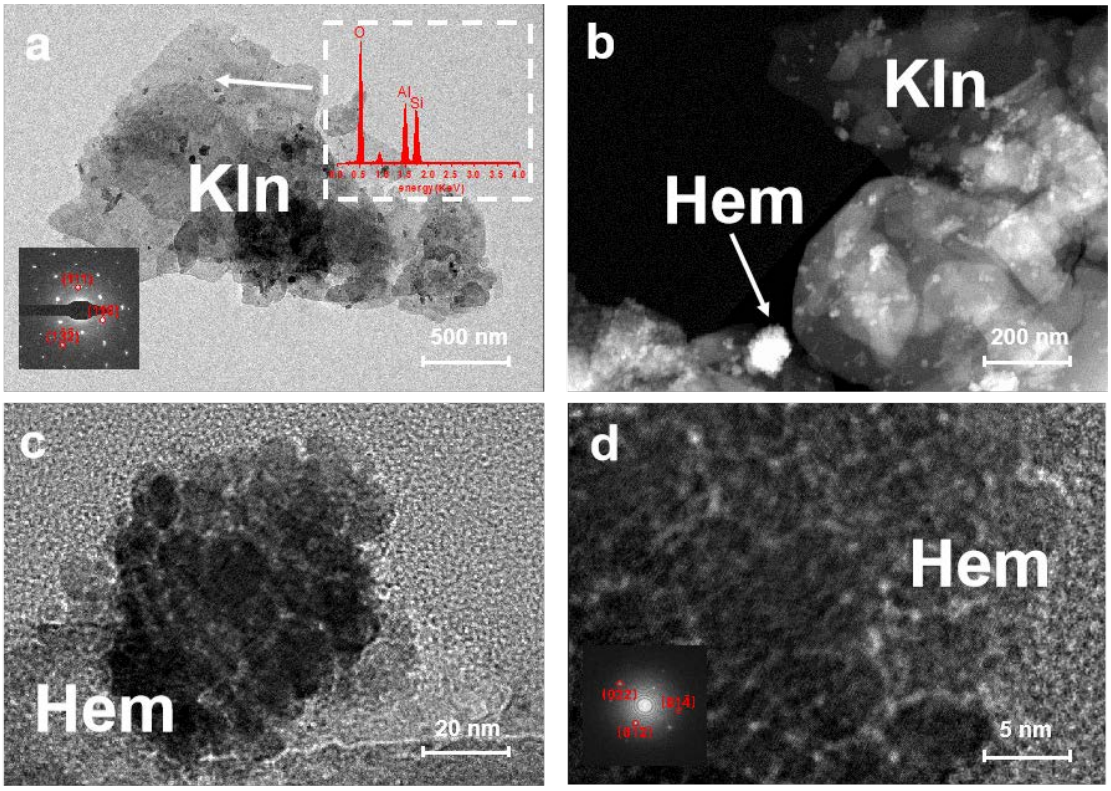

Figure 10

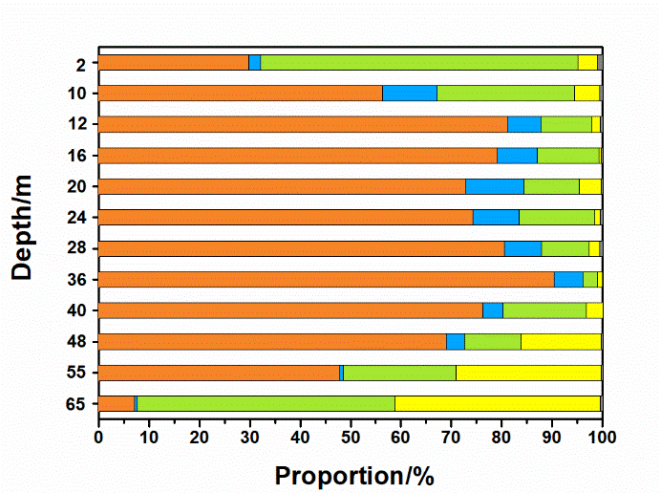

Figure 11

This is the peer-reviewed, final accepted version for American Mineralogist, published by the Mineralogical Society of America.
The published version is subject to change. Cite as Authors (Year) Title. American Mineralogist, in press.
DOI: https://doi.org/10.2138/am-2023-9217. http://www.minsocam.org/

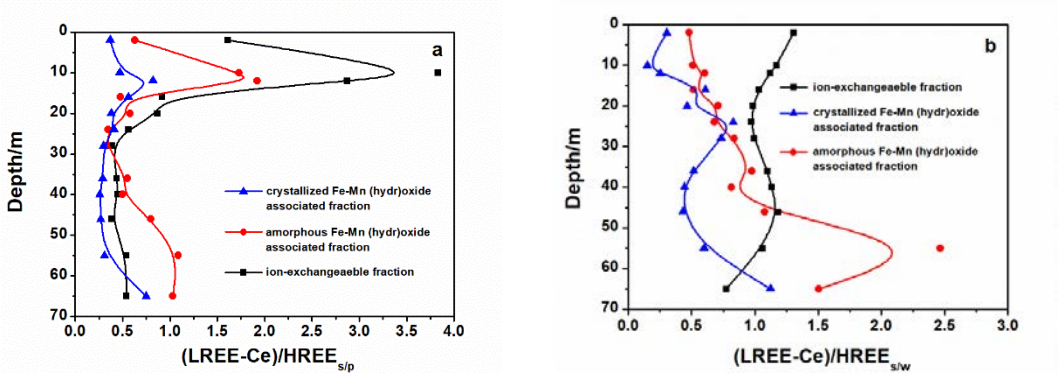

1643 **Figure 12**

1644

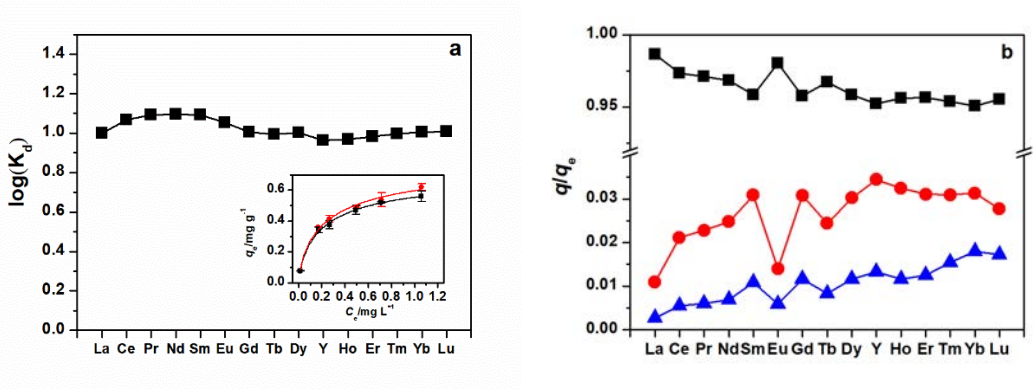

1645 **Figure 13**

1646

This is the peer-reviewed, final accepted version for American Mineralogist, published by the Mineralogical Society of America.
The published version is subject to change. Cite as Authors (Year) Title. American Mineralogist, in press.
DOI: https://doi.org/10.2138/am-2023-9217. http://www.minsocam.org/

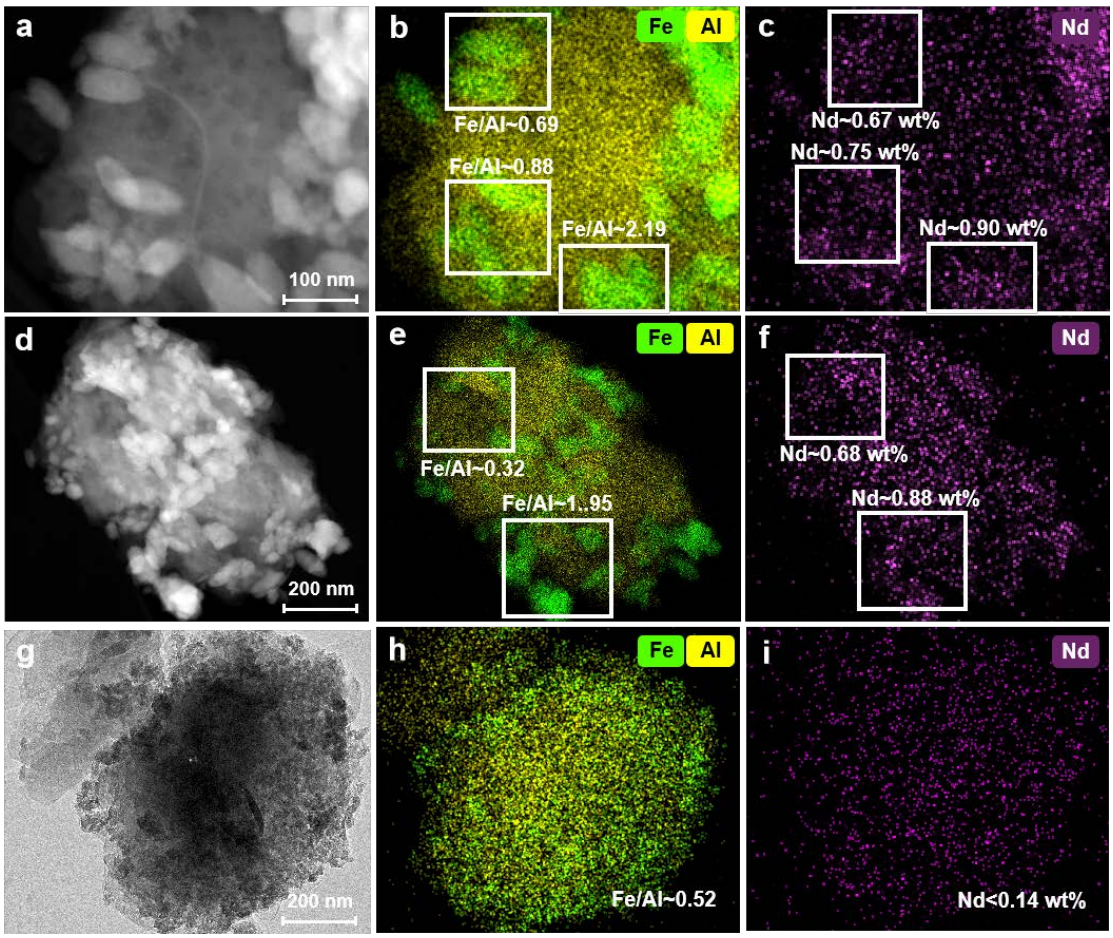

Figure 14

This is the peer-reviewed, final accepted version for American Mineralogist, published by the Mineralogical Society of America.
The published version is subject to change. Cite as Authors (Year) Title. American Mineralogist, in press.
DOI: https://doi.org/10.2138/am-2023-9217. http://www.minsocam.org/

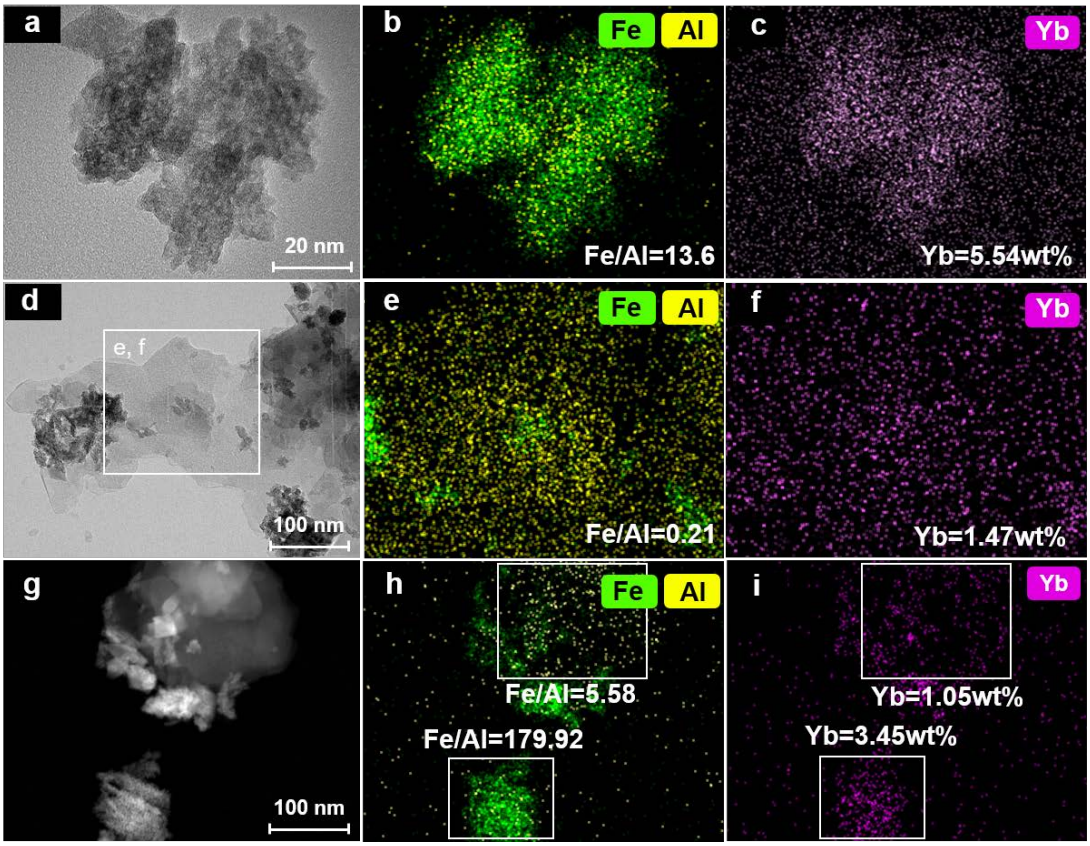

Figure 15